Measurement

3D tomographic reconstruction of light emission density of plasma in the PROTO-SPHERA experiment

--Manuscript Draft--

Manuscript Number:	MEAS-D-24-11112R1
Article Type:	Research Paper
Keywords:	3D image reconstruction; magnetically confined plasma; nuclear fusion; monitoring
Corresponding Author:	Annamaria Pau Sapienza University of Rome Rome, ITALY
First Author:	Annamaria Pau
Order of Authors:	Annamaria Pau
	Shayesteh Naghinajad
	Franco Alladio
	Paolo Micozzi
	Luca Boncagni
Abstract:	We apply a method to reconstruct 3D density functions based on a corollary of the 3D Fourier slice theorem. This corollary, proved here in its general form, links the projections of a 3D density function onto planes to the 3D Fourier transform of the density function itself. By performing a coordinate transformation and calculating the 3D inverse Fourier transform, we directly solve the inverse problem of reconstructing the density function from its projections. This method is used to represent the visible light emission density distribution of magnetically confined plasma, based on experimental data collected by ENEA for the PROTO-SPHERA project. Emissions from Helium and Hydrogen plasma are captured by cameras arranged in cylindrical symmetry. The technique allows observation of the self-organization process of a plasma torus around a centerpost, confirming theoretical predictions, and enables visualization of plasma cross-sections, revealing its internal organization and emission spectrum.

Dipartimento di Ingegneria
Strutturale e Geotecnica

Sapienza
Università di Roma

Rome, 30th of April 2025

Dear Editor

We are submitting a revision of the work titled *3D tomographic reconstruction of light emission density of plasma in the PROTO-SPHERA experiment* for consideration for publication in Measurement. In the revised version of our manuscript, all the changes are indicated with bold fonts, with additions further highlighted in yellow. No significant deletions were made. The revised version includes all the changes suggested by the reviewers, as listed here below.

The abstract was revised to include a brief but informative background that sets the context of the study.

Section 1 Introduction has been revised to remove repetitions, due to the introduction of Section 2, titled *Application of tomography to fusion diagnostics*. Moreover, several sentences in the introduction as well as in Sections 3.1 (lines 191-193) and 3.2 were modified to more accurately position our work within the context of international literature.

Section 2, titled *Application of tomography to fusion diagnostics* was added to improve completeness of the literature review. References [6], [9], [19], [23], [30], [32] and [33] were also added. In lines 114-123 of Section 2, we explained the difference of PROTO-SHERA with respect to classical tokamaks and motivated the choice of the method. At the end of Section 2, lines 124-125 and 134-136, the main contributions of the manuscript were better presented to make them more explicit and easily identifiable.

Figure 4 was added to schematically describe how the corollary of the Fourier theorem is applied to 3D-reconstruct the image. Some further explanations of the method were added to Section 3.3, lines 258-266.

In Section 4.1 *The PROTO-SPHERA experiment*, we substituted Figure 9a with a picture that shows the metal supports of the vessel to motivate some reflections observed in the image reconstruction.

In Section 4.2 *Results and discussion*, for the sake of completeness and comparison, we have added Figure 17 which replicates a figure from the paper by Damizia et al., belonging to our same research group. This figure enables comparison of our results with those obtained with a different method of reconstruction. Should the manuscript be accepted, we will formally request permission from the respective publisher to reproduce this figure.

We read the journal's policy on machine learning/ neural networks papers on the page https://www.sciencedirect.com/journal/measurement/about/policies

We also declare that in this paper we made no use of generative artificial intelligence. The material presented is the authors' original work and has not been submitted for evaluation elsewhere.

We thank you in advance for your time and consideration.

Yours sincerely,

Annamaria Pau,
Associate professor of Structural Mechanics
Department of Structural and Geotechnical Engineering
Università di Roma La Sapienza
Via Eudossiana 18 - 00184 Roma, Italy
annamaria.pau@uniroma1.it

Highlights (for review, without author details)

- Method based on the 3D Fourier slice theorem employed to reconstruct density functions from projection data
- Six-camera setup achieves accurate 3D plasma light emission density reconstruction over time
- Technique reveals hidden core emissions, previously obscured by outer plasma layers
- Plasma torus arrangement around a centerpost observed, evolving within 8 ms

Authors' Response to Reviewers of

3D tomographic reconstruction of light emission density of plasma in the PROTO-SPHERA experiment

Manuscript ID MEAS-**D-24-11112**

LEGEND: *Reviewer comment* **(RC)**, Authors' response **(AR)** and changes to the text. At the end of the response to the Reviewers, five pictures are reported to better respond to the Reviewer's comments.

In the revised pdf, all the changes are reported in **bold** fonts, with the additions highlighted in yellow.

AUTHORS' RESPONSE TO REVIEWER #1

RC *First and foremost, the validity of the Fourier slice theorem in higher dimensions is well known, and the proof can be found in computed tomography textbooks [1] (see Chapter 8), it is not a novel or original method*

AR We sincerely thank the Reviewer for their insightful criticism and literature suggestions, which helped us to better place of our contribution within the framework of the scientific literature. We acknowledge that the validity of the Fourier slice theorem in higher dimensions is well known, and was formulated by Radon himself. In fact, besides that, we had already cited Zosso's work. In comparison with Buzug's proof [1], we have resolved the ambiguity concerning the rotational degree of freedom about the detector's normal (mentioned at the end of page 330 in Buzug's book) in a different way. We attached the coordinate system to a plane tangent to a sphere, with coordinate axes aligned with the outward normal and the tangents to parallels and meridians (as shown in our Figure 3). The result is obviously the same.

This is specified in Section 3.1, lines 191-193. In addition to adding Buzug's book to the references, we have revised several sentences in the introduction as well as in Sections 3.1 and 3.2 to more accurately position our work within the context of the international literature.

RC *the method is rarely used due to artefacts in back projections (visible in all reconstruction figures 15-17).*

AR. In fact, the complete suppression of artifacts in the reconstructed image cannot be guaranteed by any method, even for a perfectly calibrated, noiseless detection system. We agree that the solution algorithms that work best in medical tomography are not necessarily the most useful for tokamak plasmas. In tokamaks, X-ray emission is measured from pinhole cameras that are not equally spaced and do not provide views from the internal surface of the torus, which is not accessible. This makes the analytical methods less appropriate for image reconstruction than finite element techniques.

However, the geometry of PROTO-SPHERA is rather different from that of a tokamak. In PROTO-SPHERA, visual access to the plasma is unhindered from any angle. The visible light emission is measured with regular cameras. In this case, 3D analytical methods can be a viable strategy for image reconstruction. While we acknowledge that our image reconstruction is not perfect and that several improvements could be made, this work represents a first step toward 3D reconstruction of the plasma visible light emission density, which has never been attempted before. Fusion plasma tomography, to the best of our knowledge, was only carried out on sections of the torus.

We would like to mention that the angle brilliance visible at the four corners, reported in Figure 1 a at the end of this response, is not an artifact, but it is due to the reflection of light from four metal columns supporting the vessel, shown in Figure 1 b. This picture has been used to better depict the setup in Figure 9a of the manuscript. In addition, we managed to reproduce the presence of some real parts of the machinery whose presence is unquestionable. This is shown in Figure 2, which shows the image of external conducting copper bars (3 cm in diameter) that connect the two electrodes, as well as the Langmuir probe immersed in the plasma. This was already displayed in Figure 14 and commented in Section 4.2, lines 378-380.

Some artifacts are certainly due to the use of a reduced number of cameras, a problem which will be addressed in future work. Anyway, in our opinion, the macroscopic phenomena that we observed are not affected by the artifacts.

In the new Section 2 concerning literature on plasma tomography, we better explained the difference of PROTO-SHERA with respect to classical tokamaks and motivated the choice of the method (lines 114-123). In Section 4.1 "The PROTO-SPHERA experiment", we modified Figure 9a with a picture showing the metal supports of the vessel.

RC *The authors spend much of the introduction on the history of medical tomography and provided no reference to related fusion plasma tomography works, just to list a few [2-6].*

References:
[1] Buzug T 2008 Computed Tomography (Berlin, Heidelberg: Springer)
[2] Granetz R S and Smeulders P 1988 X-ray tomography on JET Nucl. Fusion 28 457
[3] Mlynar J, Craciunescu T, Ferreira D R, Carvalho P, Ficker O, Grover O, Imrisek M, Svoboda J, and JET contributors 2019 Current Research into Applications of Tomography for Fusion Diagnostics J. Fusion Energy 38 458-66
[4] Anon 2017 Deep learning for plasma tomography using the bolometer system at JET Fusion Eng. Des. 114 18-25
[5] Anon 2012 Modern numerical methods for plasma tomography optimisation Nucl. Instrum. Methods Phys. Res. Sect. Accel. Spectrometers Detect. Assoc. Equip. 686 156-61
[6] Jardin A, Bielecki J, Mazon D, Peysson Y, Król K, Dworak D and Scholz M 2021 Implementing an X-ray tomography method for fusion devices Eur. Phys. J. Plus 136 706

AR Thank you for this comment. To improve completeness of the literature review, we introduced Section 2, titled *Application of tomography to fusion diagnostics*, where we comment on the manuscripts you suggest (lines 74-103), which were added among the references ([6], [19], [23], [30], [32], [33]).

RC *Secondly, the acquisition geometry is quite confusing, as the method requires parallel beams, but the actual camera acquisition is of cone beam geometry,*

AR In cone beam X-ray tomography, the radiation source is acquired by pinhole cameras and captured by the detector. The image is formed without passing through lenses. In this case, acquisition indeed needs that cone beam geometry is used.

In the case of a traditional photographic or video camera, however, the acquisition geometry is not exactly conical. The light rays entering the lens are typically treated as if they are coming from a three-dimensional scene and are focused onto the sensor's surface. The camera lens, which is a curved lens, is designed to gather the light and focus it onto a single point on the sensor. The lens converts the rays coming from different directions so that they are correctly mapped onto the sensor so that the resulting image is sharp. In addition to that, in our case, the distance of the plasma from the objective is such that perspective effects can be ignored. Moreover, a small aperture was used to get a great depth of field, so that all the field of interest appears in focus.

So, your point is correct for applications such as X-ray tomography, but does not apply to our problem, in which case, parallel projections can be used.

We better explained this point in Section 2, lines 119-123.

RC *and even more confusing is the placement of the cameras, which are all 180 degrees opposite to each other, providing essentially three views [1].*

AR: While it is true that, in an ideal scenario free from errors, two cameras placed exactly 180 degrees apart would provide redundant information, real-world measurements are inevitably affected by several sources of error. These include, but are not limited to, slight misalignments in camera positioning, optical distortions, thermal expansion, structural vibrations, and electronic noise. In this context, having views from opposite sides of the plasma is rather advantageous, as it increases the robustness of the reconstruction and helps mitigate the effects of such errors.

We added an explanation in Section 4.2 where we motivated the choice for the camera arrangement (lines 319-328).

RC *Given such limited data and the method in the manuscript, it is highly unlikely that the reconstructed profile is accurate. Although the subject is interesting, the specific method used in this manuscript is not state of the art and should not be used. I recommend that the authors read related reactor tomography work and use another reconstruction method on the acquired images and resubmit the manuscript.*

AR We thank the reviewer for the comments and would like to clarify some key aspects of our work. We acknowledge that other tomographic reconstruction techniques are available, and that in all techniques sparsity of data is a relevant issue. To deal with it, regularization techniques are a viable strategy in the case of iterative or finite element approaches, as explained in the papers that this reviewer has indicated. Despite not being explicitly declared in the initial version of our manuscript, a similar problem had to be faced in our approach. In fact, computation of the inverse 3D Fourier Transform requires a regular cubic grid of points where the function to be inverted is known, while the points where the function is actually known are in general arranged in a spherical (cylindrical in the case of PROTO-SHPERA) grid. To obtain the values on the cartesian grid, the data available on the cylindrical grid was linearly interpolated, which – broadly speaking - provides a form of regularization. This point was clarified in Section 3.3 lines 258-266 of the present manuscript.

However, rather than developing a novel tomographic method, our primary objective was instead to prove applicability of existing methods used in other fields, to the peculiar case of PROTO-SPHERA, which differs from the tokamaks for the accessibility of the plasma in terms of diagnostics and for the nature of the signal treated (light instead of X-rays), and in particular to investigate physics of the plasma formation dynamics. This point was clarified in Section 2 of the present manuscript, lines 124-125 and 134-136. Despite the relatively simple reconstruction approach employed, the results are consistent with both theoretical predictions and experimental observations in the literature and are not affected by artifacts that could compromise their interpretation.

Our analysis shows that the plasma torus forms in approximately 8 milliseconds, evolving from a kinked filament generated by the destabilization of the central plasma column. The cross-sectional views reveal a previously unreported green light emission from the core, while equatorial sections enable a rough estimate of the torus thickness.

These findings align closely with predictions from magnetohydrodynamic (MHD) models, in particular those presented in the work by Garcia-Martinez, Lampugnani, and Farengo (Physics of Plasmas, 2014). Figure 3 of this letter compares Figure 13 of the manuscript with Figure 9 from Garcia-Martinez et al., which shows magnetic field lines at different Lundquist numbers. The topological similarity between the two sets of results is evident. Likewise, Figure 4 of this letter compares Figure 16 of the manuscript—depicting the emission density in the equatorial plane—with Figure 8(B) from the same reference, which shows the ratio between current density and magnetic field. Both figures display remarkably similar morphologies, featuring a centerpost around which a toroidal structure forms.

Further experimental confirmation comes from the PROTO-SPHERA research group, who obtained similar results using different reconstruction techniques. Specifically, Figure 5 of this letter shows plasma luminosity obtained through tomographic inversion using Zernike polynomials, as reported in the work by Damizia et al. (*Optical Tomography of the Plasma on the PROTO-SPHERA Experiment*, 2021), which is reference [9] of the amended manuscript. Although the data in this figure refer to earlier experiments conducted with Argon gas and are not shown in true color, they support the presence of the toroidal light emission structure and of the centerpost observed in our study. We would like to underline that the data used by Damizia et al. were not used in the manuscript under review, as they correspond to an earlier phase of the experimental campaign during which several setup details were still being finalized.

For the sake of completeness and comparison, we have also included Figure 17 taken from the paper by Damizia et al. in the revised version of the manuscript. Should the manuscript be accepted, we will formally request permission from the respective publisher to reproduce this figure.

We would also like to stress that, to the best of our knowledge, this work represents the first attempt to reconstruct the three-dimensional visible light emission density of a plasma. Traditional approaches to plasma tomography have typically focused on cross-sectional reconstructions of toroidal structures.

In conclusion, although we recognize that the reconstruction method used might not be state of the art, we believe that the physical insights and experimental observations presented in our study are significant and well-supported. We hope that the reviewer will reconsider the value of our work in light of the arguments and evidence outlined above.

AUTHORS' RESPONSE TO REVIEWER #2

RC *The abstract would benefit from additional background information and a clearer articulation of the manuscript's contributions.*

AR We thank the reviewer for this suggestion. In response, we have revised the abstract to include a brief but informative background that sets the context of the study. Additionally, we have clarified the main contributions of the manuscript to make them more explicit and easily identifiable in Section 2, lines 124-125 and 134-136.

RC *Certain sections (e.g., around lines 16-17) are missing citations, and the discussion of related work should be organized into a dedicated section for better clarity.*

AR To improve completeness of the literature review, we introduced Section 2, titled *Application of tomography to fusion diagnostics*. References [6], [9], [19], [23], [30], [32] and [33] were added and discussed. Consequently, the introduction has been revised to remove repetitions.

RC *A detailed pipeline describing the methodology would help improve the transparency and comprehensibility of the process.*

AR The methodology works as follows. The vertical projection of the points of the density function $f(x, y, z)$ onto an arbitrarily angulated detector plane are obtained. The projection containing all line integrals perpendicular to the projection plane is $P_{\theta,\phi}(t,r)$. A two-dimensional Fourier transform from the plane (t,r) to the domain (μ, ν) yields $[F_2 P_{\theta,\phi}](\mu, \nu)$. This plane can be sorted into the (u,v,w) wavenumber space with a transformation of coordinates. If the projections have been measured for all angulations, then the object can finally be reconstructed by means of the inverse three-dimensional Fourier transform. In the case of a finite number of projections, we need to retrieve the data onto a regular 3D cartesian grid of wavenumbers, 3D Fourier invert and then obtain an approximation of the original density.

Figure 4 describing schematically how the corollary of the Fourier theorem is applied to 3D-reconstruct the image is reported in Section 3.2. Some further explanations were added in Section 3.3, lines 258-266.

RC *Experimental comparisons with existing methods are necessary to validate the effectiveness of the proposed approach.*

Experimental comparison comes from the PROTO-SPHERA research group, who obtained similar results using different reconstruction techniques. Specifically, Figure 5 of this response letter shows plasma luminosity in false colors obtained through tomographic inversion using Zernike polynomials, as reported in the work by Damizia et al. (*Optical Tomography of the Plasma on the PROTO-SPHERA Experiment*, 2021), which is now reference [9] of the revised manuscript. Although the data in this figure were obtained in earlier experiments conducted with Argon gas, they support the presence of the toroidal light emission structure and of the centerpost observed in our study. These data were not used in the manuscript currently under review, as they correspond to an earlier phase of the experimental campaign during which several setup details were still being finalized.

For the sake of completeness and comparison, we have added Figure 17, taken from the paper by Damizia et al. for comparison. Should the manuscript be accepted, we will formally request permission from the publisher to reproduce it.

FIGURES

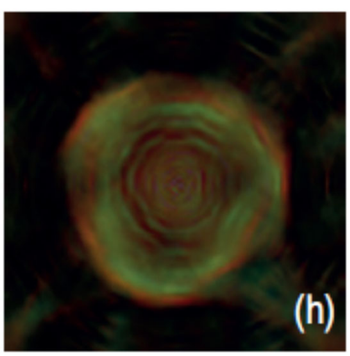

a)

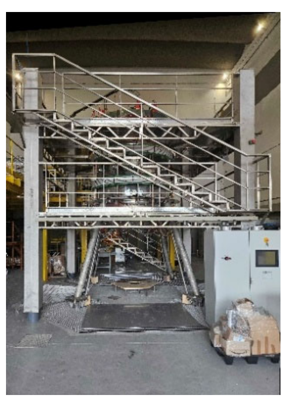

b)

Figure 1: Cross-section of plasma with angle reflections a) and structure supporting the vessel

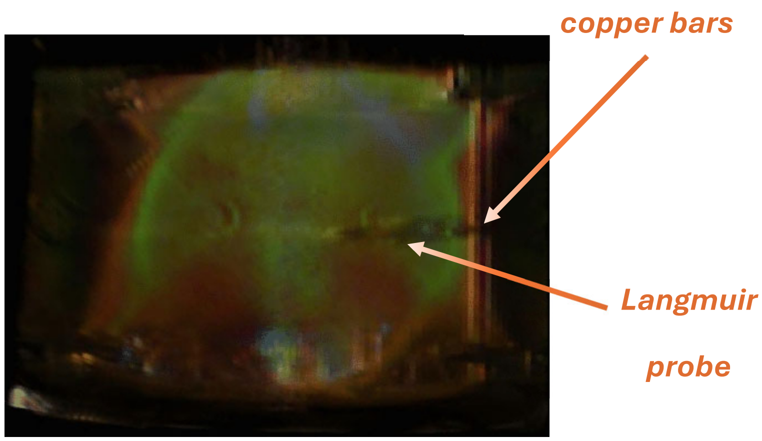

Figure 2 Vertical section of the plasma displaying the Langmuir probe and the copper bars

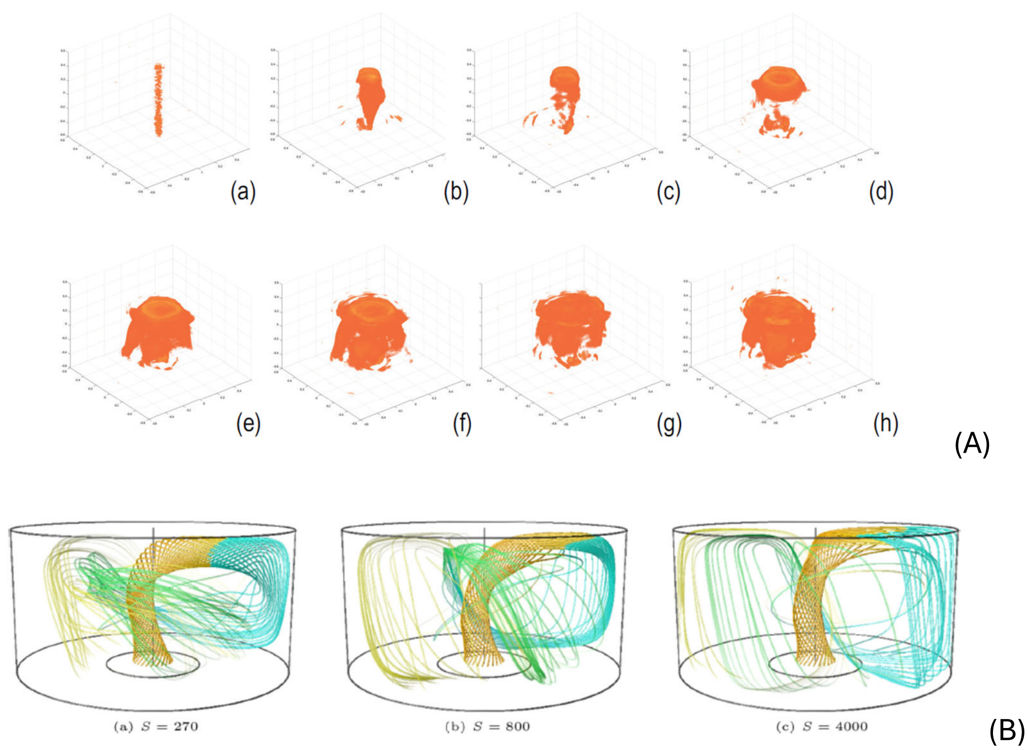

Figure 3: comparison of Figure 13 of the submitted manuscript (A) with Figure 9 (B) of the paper by Garcia-Martinez et al., which represents the field lines of the magnetic field at different Lundquist numbers.

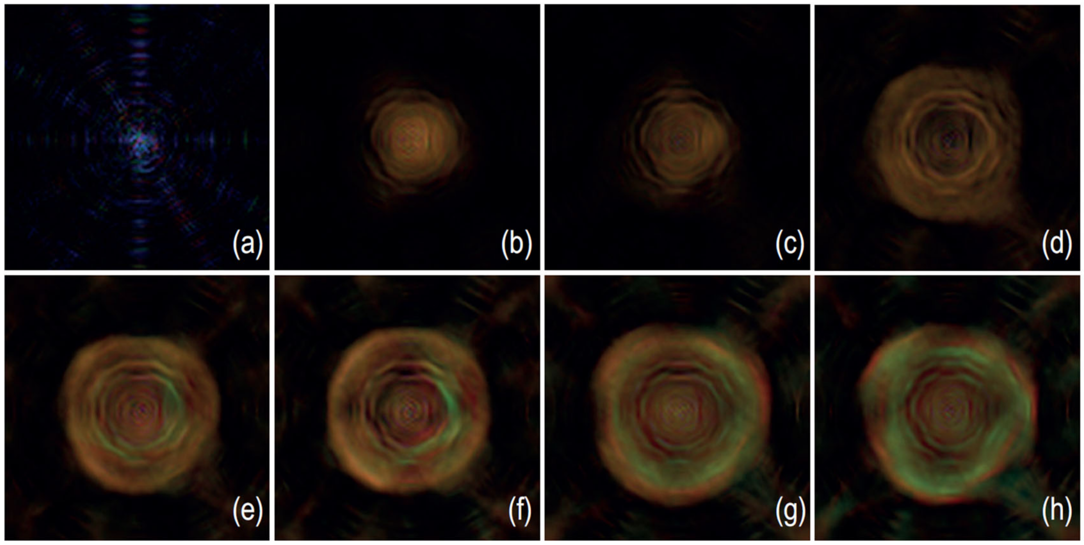

(A)

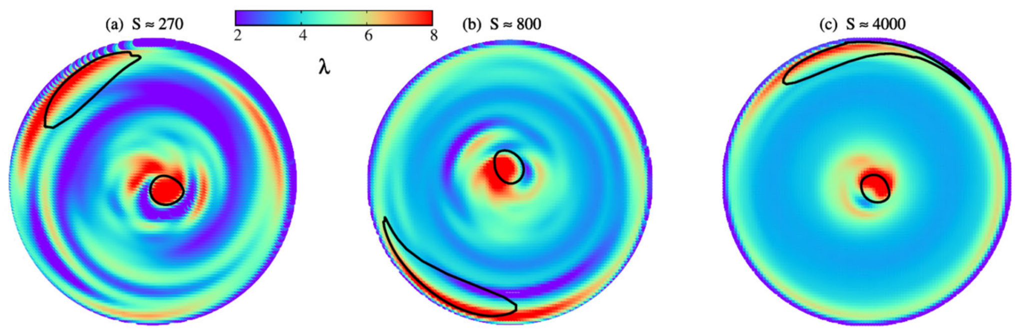

(B)

Figure 4 comparison of Figure 16 of the submitted manuscript (A) with Figure 8 (B) of the paper by Garcia-Martinez et al., representing the contourplot of the ratio between current density and magnetic field at different Lundquist numbers

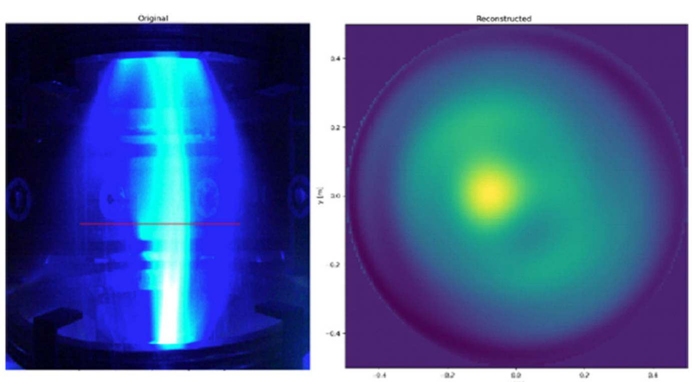

Figure 5 Picture and related equatorial distribution of Argon plasma luminosity obtained by Zernicke polynomials inversion (Y. Damizia et al. Optical tomography of the plasma on the PROTO-SPHERA experiment (2021))

3D tomographic reconstruction of light emission density of plasma in the PROTO-SPHERA experiment

Abstract

We address a key challenge in plasma diagnostics: reconstructing the three-dimensional (3D) light emission density from projection data. To this end, we employ a method for reconstructing 3D density functions based on a corollary of the 3D Fourier slice theorem. This corollary establishes a connection between 2D plane projections and plane sections of the 3D Fourier transform, enabling a direct and non-iterative solution to the inverse problem. The method is applied to the PROTO-SPHERA experiment, an innovative magnetic confinement plasma setup for controlled nuclear fusion research. Experimental data were acquired using six high-speed cameras arranged with cylindrical symmetry around the plasma chamber, capturing time-resolved pictures that are assumed to be parallel projections of the visible light emissions from Helium and Hydrogen discharges. After a transformation of coordinates, by computing their inverse 3D Fourier transform, we reconstruct the spatial distribution of light emission density. This technique enabled to reveal dynamic features of plasma self-organization—such as torus formation around a centerpost—and provides internal cross-sectional views of the plasma, displaying previously obscured spectral components.

Keywords: 3D image reconstruction, magnetically confined plasma, nuclear fusion, monitoring

1. Introduction

Tomographic computed (CT) imaging or scanning is a technique of data treatment which enables visualization of the inner part of objects instead of making real cuts. This has obvious and important applications in the medical field, as well as in the nondestructive monitoring of structures and industrial processes. CT requires the solution of an inverse problem, which can be formulated as follows: given the knowledge of some data called projections, reconstruct the spatial distribution of a density function $f(x, y, x)$ which represents some property (for instance mass density) of an object in the 3D space. Projections are obtained by illuminating the object with stimuli which produce a measurable response, which is measured on the object boundary. Projections are, in practice, a sort of shade that the function $f(x, y, x)$ projects onto lines, or planes. The mathematical demonstration that a density function could be reproduced from an infinite set of its projections was provided by the mathematician J. Radon [37] at the beginning of last century. However, it is quite remarkable that reconstruction of images from projections was not attempted until 1940. In 1972, Hounsfield [21] proposed the first method that allowed to image plane slices of the internal structure of a human body using X-rays projections. The Nobel prize in physiology and medicine in 1979 awarded to Hounsfield and Cormack [8] for their work on the initial computed tomography device signifies the importance that this technique has in the medical field. Since then, the use of computed tomography was extended to a wide number of industrial applications [10], among which food industry [38], materials science [29], geosciences [7] and **fusion diagnostics [19, 33, 30, 32]**.

Medical and industrial computed tomography is based on the same underlying principles but differs in the acquisition system layout, as well as in the stimulus that is used to obtain the projections, which is X-rays in medical CT, but can also be another physical source. In fact, the reflected or transmitted signal of any source which produces a measurable response of the scanned object can be used. The feasibility of using ultrasounds [25, 22, 26], the photo elastic effect [41], or even ground-penetrating radar emitting microwaves [1] has been proved to be effective to visualize internal patterns of objects. Different sources interact with different properties, which can include, besides mass density, electrical, acoustic, and electromagnetic properties of materials and tissues. For instance, in nuclear medicine, the interest is focused on reconstructing a cross-sectional image of radioactive isotope distributions within the human body [12], while in magnetic resonance the magnetic properties of the object is reconstructed [15]. The photelastic effect instead was used to determine the plane stress distribution in an optical fiber [35]. **The most fundamental distinction between medical CT and fusion diagnostics lies in the nature of the signal: while medical**

tomography is primarily concerned with absorption, fusion diagnostics focuses on emission. The main difference between the mentioned sources is that some of them are non-diffracting, like X-rays, which travel in straight lines [4], while some others are diffracting, like ultrasounds, that is, they are scattered in all directions, resulting in a more complex inverse problem [24].

To convert the measured response data into an image, appropriate processing is necessary. The most popular algorithms that are in use can be classified into two major categories, which are iterative and analytical methods [20]. Iterative methods are numerical reconstruction algorithms that employ a model to predict the measured data from an initial estimate and then refine the image estimate to better fit the measured data. This process is repeated iteratively until the image quality meets a predetermined standard or until further iterations do not significantly change the image [39, 40]. Starting from the Algebraic Reconstruction Technique (ART) [17], research continues to evolve with refinements and developments, such as the customized Simultaneous Algebraic Reconstruction Technique (SART) [13], and the Simultaneous Iterative Reconstruction Technique (SIRT) [42]. Analytical algorithms are based on mathematical models and explicit formulas that directly compute the image from the acquired projection data. They can be further categorized into two groups: the direct or Fourier-Transform-based methods [43, 18] and the Back-Projection-based algorithms, like Simple Back Projection (SBP), Linear Back Projection (LBP) and Filtered Back Projection (FBP) [34, 42]. Fourier-Transform-based algorithms rely on the relationship between the Fourier transform (FT) of the image and the Fourier transform of its projections. More specifically, projections are obtained using Radon transforms [24], that is by computing line integrals of the density function. A more detailed discussion of the literature on the classification of CT algorithms is beyond the scope of this paper. The interested reader can consult [26, 11] for a more eshaustive presentation of the matter.

2. Application of tomography to fusion diagnostics

In tokamaks, reconstruction of X-ray emission relies on data collected by line-integrated detectors — such as pinhole X-ray cameras, bolometers, and neutron cameras— arranged across a cross-section of the plasma. Unlike medical imaging systems, which benefit from unrestricted access to the subject from all angles, fusion

diagnostics is constrained by the geometry of the tokamak. The number and placement of detectors are limited by the physical design of the device, leading to a much lower spatial resolution than that achievable in medical tomography. As a consequence of this sparse and uneven data, plasma tomography requires additional assumptions, such as smoothness or regularity of the emission field, regardless of the inversion technique employed [23].

Under these circumstances, analytical and iterative methods faced various challenges, prompting the development of dedicated numerical techniques specifically tailored for 2D cross-sectional plasma tomography. These numerical approaches rely on an algebraic formulation of the image reconstruction problem, where each equation represents the equality between a known measured integral and the sum of emissions along a corresponding line of sight. However, the resulting system is typically underdetermined and the problem ill-posed, with high sensitivity to data error. To address this issue, various regularization techniques are employed to constrain the solution space, often by promoting smoothness or limiting complexity in the results. Among the robust regularization methods used in plasma tomography, Tikhonov regularization, Maximum Likelihood estimation, and Fisher information-based approaches are particularly noteworthy [32, 30]. In addition, there have been efforts to apply neural networks and deep learning techniques to tomographic reconstruction, offering promising alternatives for handling the inherent challenges of the problem [33].

In this work, we aim to apply tomographic techniques to reconstruct the light emission density recorded during the PROTO-SPHERA experiment deployment [2], conducted at the ENEA laboratories (Italian National Agency for New Technologies, Energy and Sustainable Development) in Frascati, Italy. During the experiment, the plasma emits photons, whose light is captured by six cameras arranged with cylindrical symmetry. PROTO-SPHERA is an innovative magnetic confinement plasma experiment designed for research in controlled thermonuclear fusion. Its goal is to form a plasma torus not around a solid metal centerpost, as in traditional tokamaks, but around a plasma centerpost. This setup introduces significant differences compared to the reconstruction of X-ray emission density in tokamaks. Firstly, PROTO-SPHERA

provides unobstructed visual access from any viewing angle. Secondly, the plasma produced by PROTO-SPHERA has emission concentrated in the visible and ultraviolet spectrum. Last but not least, the optical system uses lenses, producing a sharp image with limited perspective effect, due to the distance between plasma and cameras. The image that can then be treated as a parallel projection of light emission.

To the best of our knowledge, fusion plasma tomography, was only carried out on sections of the torus. Here, we employ the imaging technique based on a corollary to Fourier slice theorem in 3D, also called Fourier Section Theorem [6, 44] and based on an nth-dimension formulation of the Radon transform, provided by Radon himself: by calculating 3D inverse Fourier transforms of 2D Fourier transforms of plane projections, the 3D image of the scanned object can be reconstructed. This differs from the classical tomographic approach [28, 14], where a 3D image is reconstructed by assembling stacks of images deriving from of reconstructed images on several parallel planes. This work represents a first step toward 3D reconstruction of the plasma visible light emission density, which has never been attempted before. The resulting images enabled the observation of important aspects of plasma formation and arrangement.

This paper is organized into two sections: **Section 3 revises the method of image reconstruction in 3D based on a corollary of the Fourier slice theorem, and Section 4 reports the experimental results. For the ease of the reader, in Subsection 3.1,** the 3D continuous Radon transform is recalled, then in Subsection 3.2 the lemma of the Fourier slice theorem that is at the base of the image reconstruction method employed is **presented**. In Subsection 3.3 proof of the effectiveness of the reconstruction method is provided by using numerical data. Subsection 4.1 describes the PROTO-SPHERA experiments, and Subsection 4.2 illustrates how the tomographic reconstruction enabled to prove the sustainment of the plasma torus around the centerpost and provided further useful information on the dynamics of confined plasma.

3. Analytical direct 3D image reconstruction

3.1. 3D continuous Radon Transform

For simplicity's sake, the 2D Radon transform is first introduced. Let us consider a plane object - or a slice of a 3D object - with density function $f(x, y)$ (Figure 1). Its projections onto a line inclined by an angle θ with respect to the x axis are obtained by integrating $f(x, y)$ on the set of parallel lines (rays) that are inclined by an angle $\theta + \pi/2$ with respect to the x axis and at a distance t from the origin of the coordinate system (bold line in **Figure** 1). The equation of a ray is:

$$t = x\, cos\theta + y\, sin\theta. \tag{1}$$

The projection of the function $f(x, y)$ is then defined as:

$$p(\theta, t) = \int_{-\infty}^{\infty} \int_{-\infty}^{\infty} f(x, y)\delta(x\, cos\theta + y\, sin\theta - t)dxdy, \tag{2}$$

where δ is the Dirac's delta function. Equation (2) represents the 2D continuous Radon transform $[\mathcal{R}_2 f](\theta, t)$ of the function f, which is depicted schematically in Figure 1 by the blue curve subtending the sky blue area. It is often preferred to integrate in the rotated coordinate system (t, s), where the projection can be written as:

$$p(\theta, t) = \int_{-\infty}^{\infty} f(t, s)ds. \tag{3}$$

Geometrically, the continuous 2D Radon transform maps a function in $\mathbb{R}^2$ into the set of its line integrals in $\mathbb{R}^2$. The reconstructed image function $f(x, y)$ is formally obtained by inverting the Radon transform:

$$f(x, y) = [\mathcal{R}_2^{-1} p](\theta, t). \tag{4}$$

Let us now consider a 3D object with density function $f(x, y, z)$ (Figure 2). Its projections are obtained by integrating $f(x, y, z)$ on the plane Σ that is orthogonal to the versor $\boldsymbol{\alpha}$ and at a distance d from the origin of the coordinate system. The versor has direction cosines $\boldsymbol{\alpha} = (cos\theta\, cos\phi, sin\theta\, cos\phi, sin\, \phi)^T$, where ϕ is the angle that $\boldsymbol{\alpha}$ forms with the z axis, and θ is the angle that the projection of $\boldsymbol{\alpha}$ onto the xy plane forms with the x axis. The equation of a plane orthogonal to $\boldsymbol{\alpha}$ and at a distance d from the origin is:

$$d = x\,cos\theta\,cos\phi + y\,sin\theta\,cos\phi + z\,sin\phi. \tag{5}$$

In an analogy with Equation (2), the projection of the function $f(x, y, z)$ associated with the couple $(\boldsymbol{\alpha}, d)$ is then defined as:

$$p(\boldsymbol{\alpha}, d) = \int_{-\infty}^{\infty}\int_{-\infty}^{\infty}\int_{-\infty}^{\infty} f(x, y, z)\delta(x\,cos\theta\,cos\phi + y\,cos\theta\,sin\phi + z\,sin\theta - d)dxdydz. \tag{6}$$

The area over which the previous integral is computed is included in the dashed line in Figure 2. Equation (6) represents the 3D continuous Radon transform $[\mathcal{R}_3 f](\boldsymbol{\alpha}, t)$ of the function f. Geometrically, the continuous 3D Radon transform maps a function in $\mathbb{R}^3$ into the set of its plane integrals in $\mathbb{R}^3$. The reconstructed image function $f(x, y, z)$ is formally obtained by inverting the Radon transform:

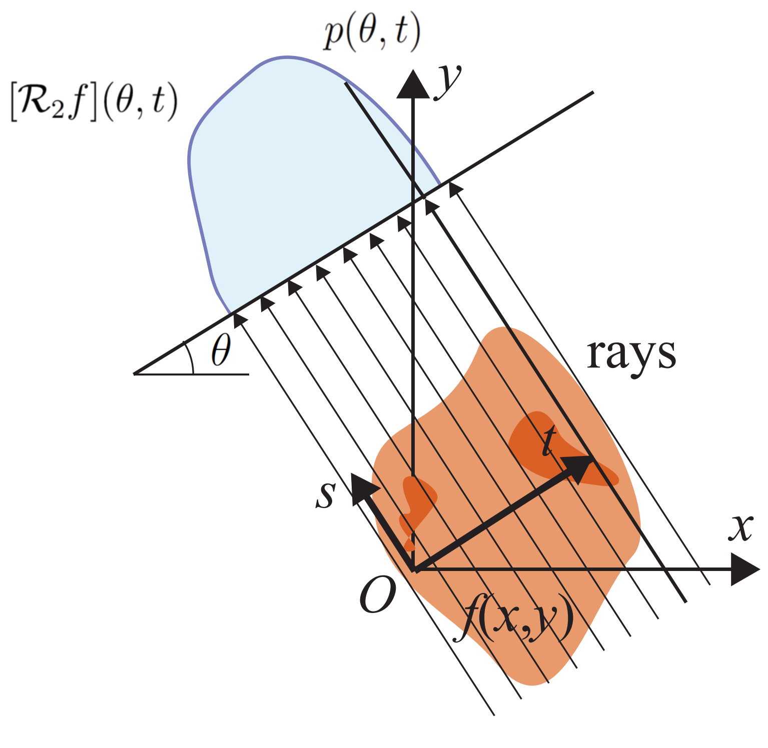

Figure 1: Projection of a plane density function onto a line.

$$f(x, y, z) = [\mathcal{R}_3^{-1} p](\boldsymbol{\alpha}, d). \quad (7)$$

It is important to note that in real applications we won't be dealing with plane integrals. In fact, $\mathcal{R}_3$ can be obtained by computing the $\mathcal{R}_2$ of the intersection between f and the plane Σ, and then integrating over lines orthogonal to the rays, which are displayed in Figure 3 as yellow lines. The line integrals are much easier to be obtained in practical measurements. They correspond to projections **onto detector planes** taken from different angles, or, in the present case, to pictures taken from different cameras.

With the definition introduced above, the detector plane still has a rotational degree of freedom around the detector normal. Different from what is done in [6], here we integrate in the rotated coordinate system (t, s, r), whose axes t and s coincide with the tangent lines to the parallels and meridians, respectively, of an imaginary sphere centered in the origin of the system of coordinates, at the point of intersection between

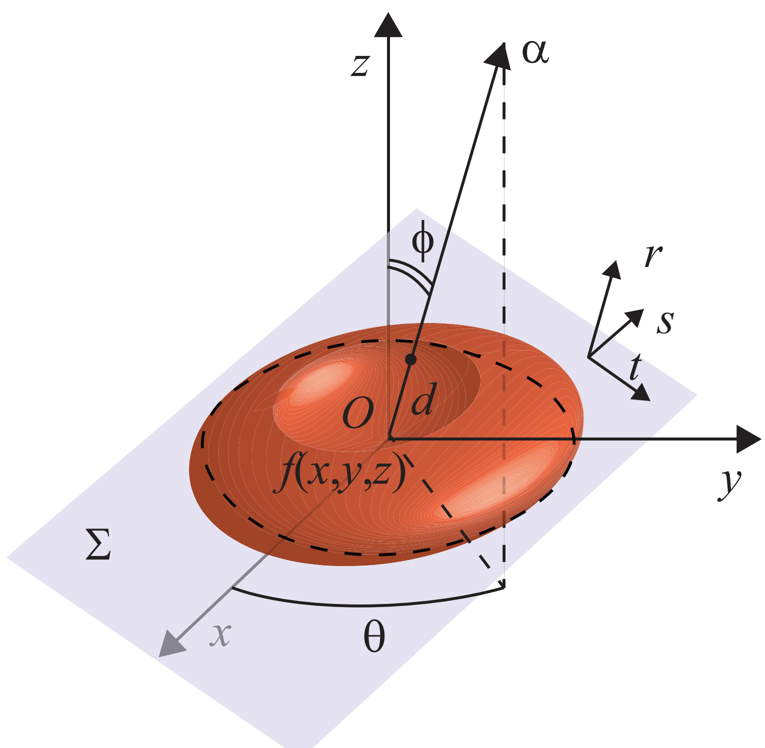

Figure 2: Projection of a 3D density function onto a plane.

the sphere and the versor $\boldsymbol{\alpha}$, with the orientation of the r axis coinciding with that of $\boldsymbol{\alpha}$ (Figure 3, upper left). **The plane (t, s) is the detector plane.** The transformation of coordinates from (x, y, z) to (t, s, r) can be written as:

$$\begin{bmatrix} t \\ s \\ r \end{bmatrix} = \begin{bmatrix} cos\phi & 0 & sin\phi \\ 0 & 1 & 0 \\ sin\phi & 0 & cos\phi \end{bmatrix} \begin{bmatrix} cos\theta & sin\theta & 0 \\ -sin\theta & cos\theta & 0 \\ 0 & 0 & 1 \end{bmatrix} \begin{bmatrix} x \\ y \\ z \end{bmatrix}. \tag{8}$$

Moreover, the distance d can be expressend in the (t, s, r) system of coordinates as $d = \sqrt{t^2 + r^2}$. The ray integral is then expressed as follows:

$$p(\theta, \phi, t, r) = \int_{-\infty}^{\infty} f(t, s, r) ds. \tag{9}$$

The integral $p(\theta, \phi, t, r)$ is in practice a line projection of the 3D function. The set of all the line projections on the plane (t, r) for given θ and ϕ will be denoted as $P_{\theta,\phi}$.

3.2. *3D Fourier slice theorem*

The extension of the Fourier slice theorem to higher dimensions, enables direct reconstruction of 3D objects. The 3D Fourier Slice Theorem can be

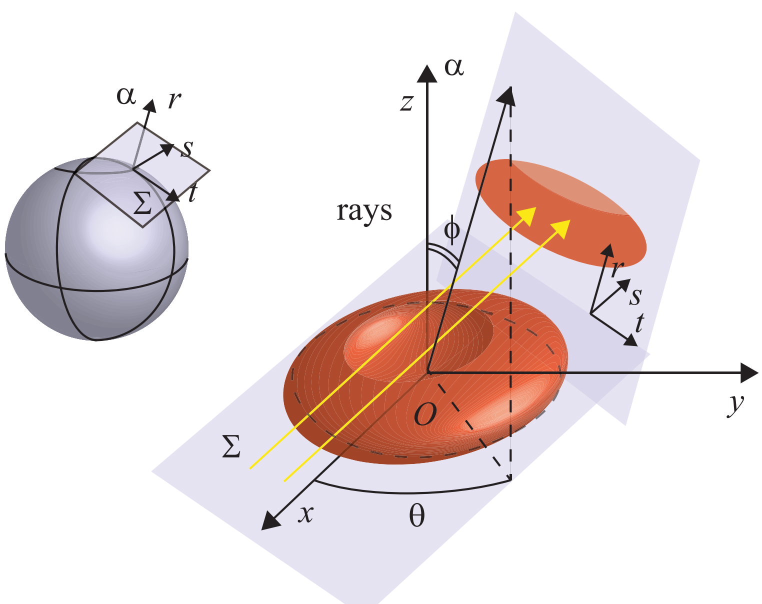

Figure 3: Ray integrals over a 3D function.

stated as follows.

Theorem 1. *A line slice of the 3D Fourier transform of the function* $f(x, y, z)$ *equals the 1D Fourier Transform of the 3D Radon transform* $[\mathcal{R}_3 f](\boldsymbol{\alpha}, t)$ *at the same angle.*

For proof, the interested reader can consult [44, 5]. However, the theorem in this form is of little use for practical purposes. A useful corollary can be stated. **See for instance [6].**

Corollary 1.1. *A plane slice of the 3D Fourier transform of the density function* $f(x, y, z)$ *equals the 2D Fourier Transform of the set of line projections at the same angle.*

Proof. Let us consider the line projection of a 3D density function $P_{\theta,\phi}$, and take its 2D Fourier Transform ($\mathcal{F}_2$):

$$[\mathcal{F}_2 P_{\theta,\phi}](\mu, \nu) = \int_{-\infty}^{\infty} \int_{-\infty}^{\infty} P_{\theta,\phi}(t, r) e^{-2\pi i(\mu t+\nu r)} dtdr, \tag{10}$$

where μ and ν are the wavenumbers in the t, r directions, respectively and i is the imaginary unit.

By substituting equation (9) into equation (10), we get:

$$[\mathcal{F}_2 P_{\theta,\phi}](\mu, \nu) = \int_{-\infty}^{\infty} \int_{-\infty}^{\infty} [\int_{-\infty}^{\infty} f(t, s, r) ds] e^{-2\pi i(\mu t+\nu r)} dtdr. \tag{11}$$

Based on the transformation (8), the rotated coordinate system (t, s, r) can be converted back into the initial (x, y, z) system:

$$[\mathcal{F}_2 P_{\theta,\phi}](\mu, \nu) = \int_{-\infty}^{\infty} \int_{-\infty}^{\infty} \int_{-\infty}^{\infty} f(x, y, z)\, e^{-2\pi i k}\, dx\, dy\, dz \tag{12}$$
$$\text{with} \quad k = \mu \cos\phi \cos\theta\, x + \mu \cos\phi \sin\theta\, y + \mu \sin\phi\, z + \nu \sin\phi \cos\theta\, x + \nu \sin\phi \sin\theta\, y + \nu \cos\phi\, z.$$

It is obvious that, **with a transformation of coordinates**, the right hand side of (12) represents the 3D Fourier Transform $\mathcal{F}_3$ of f at wavenumbers $u = \mu cos\phi\, cos\theta + \nu sin\phi\, cos\theta$, $v = \mu cos\phi\, sin\theta + \nu sin\phi\, sin\theta$ and $w = \mu sin\phi + \nu cos\phi$:

$$[\mathcal{F}_3 f](u, v, w) \int_{-\infty}^{\infty} \int_{-\infty}^{\infty} \int_{-\infty}^{\infty} f(x, y, z) e^{-2\pi i(ux+vy+wz)} dxdydz, \tag{13}$$

which proves the corollary. The quantities u, v and w are wavenumbers in directions x, y and z, respectively. $\square$

The interesting consequence of this corollary is that, given the **plane** projections, calculating their 2D Fourier Transform, **and then computing the inverse 3D Fourier Transform of the resulting set of 2D Fourier transforms after a transformation of coordinates**, the original image is directly reconstructed. **Figure 4 reports a flowchart of the described image reconstruction procedure. The following subsection provides numerical proof.**

3.3. Numerical example of the 3D direct reconstruction

Let us consider an input density function modeled as a cube with a uniform density of 0.5, side length of 0.6, and centered at the origin of the coordinate system (Figure 5a). Inside this cube, two smaller spheres are embedded: one with a density of 0.3, a radius of 0.1, and centered at coordinates (0.05, 0.05, -0.2); the other with a density of 0.1, a radius of 0.05, and centered at (-0.1, 0, 0.1). These variations in density are used to verify the accuracy of the reconstruction, ensuring it can effectively distinguish between different density regions. Although the spheres are not visible from the exterior of the solid cube, Figure 5b illustrates their positions by rendering the cube with partial transparency. It is important to note that for

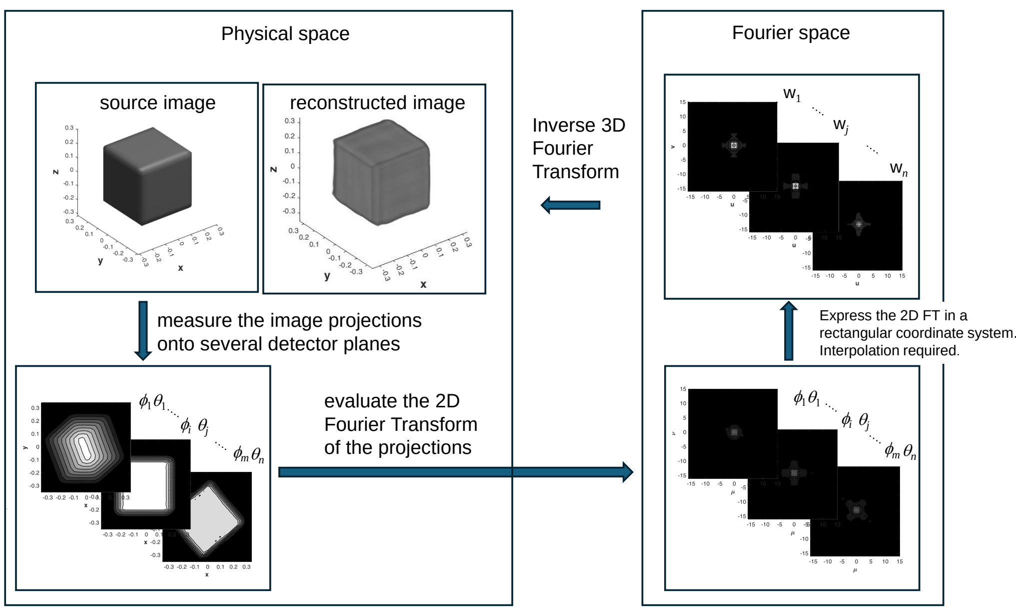

Figure 4: Flowchart of the image reconstruction procedure.

this numerical example, the theoretical framework developed for continuous systems in the previous sections has been adapted for use with discrete data. In this case, we employed a total of $N = 64 \times 64 \times 64$ sampling points, with 64 points along each side of the cube. Additionally, $N_{deg} = 12 \times 12 = 144$ spherical projections were taken, with 12 projections for each angle θ and ϕ, respectively. The angular step size was kept constant over π, set to $\pi/12$.

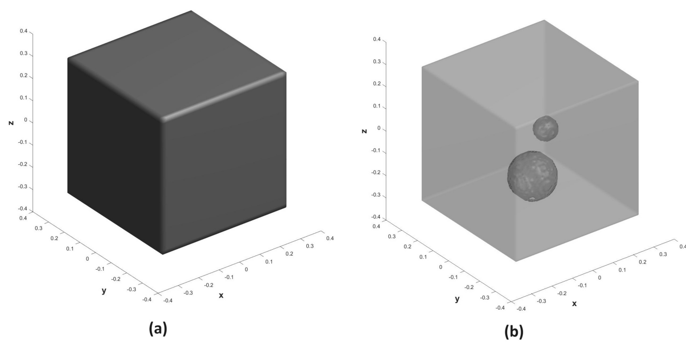

Figure 5: a) 3D density function b) density function made partially transparent to show the embedded spheres

Figures 6a and b provide samples of the spherical projections used for reconstruction, taken at angles $(\theta, \phi) = (\pi/2, 0)$ and $(2\pi/3, 0)$, respectively. Note that the color scale extends beyond 0.5 because it represents line integrals of the density function over the entire domain, rather than local values. Regions of lower density show in fact lower integral values. **At this point, it is nexessary that 144 2D Fourier Transforms of the spherical projections are computed. These Transforms are defined on the plane (μ, ν) (Equation (11)). However, computing the inverse 3D Fourier Transform requires knowledge of the data on a Cartesian grid of wavenumbers (u, v, w) (Equation (12)). Therefore, after the transformation of coordinates, discrete data available has to be interpolated to obtain the values onto a regularly spaced Cartesian grid, then 3D inverted. In this way,** the reconstructed density function shown in Figure 7a is obtained, matching the original function from Figure 5a. Figures 7b, c, and d present cross-sections of the reconstructed density function along two vertical planes (b,c) and a horizontal plane (d) passing through the origin, with the corresponding color scale. This Figure shows that the embedded spheres are exacly reconstructed not only in terms of position, but also in terms of density. See in fact that the large sphere has high density, while the small one low.

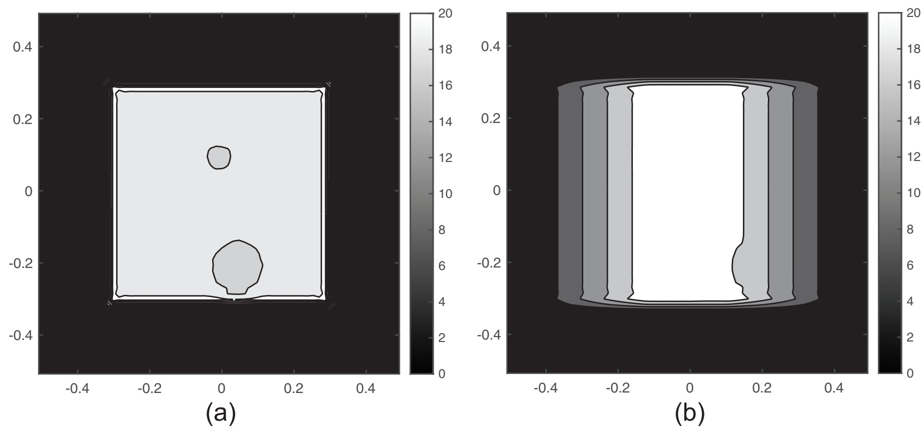

Figure 6: A couple of spherical projections pertaining to angles a) $\theta = \pi/2$, $\phi = 0$ and b) $\theta = 2\pi/3$, $\phi = 0$

The previous example was implemented using a large number of projections. While reducing the number of projections results in a slightly blurred reconstructed image, even a very limited number of projections still provides a sufficiently clear reconstruction. This effect is illustrated in Figure 8, which shows the reconstructed density function with varying numbers of projections. The source density function is depicted in Figure 8 (a). It is shaped as a cube with a unit density, a side length of 0.2, and is centered at the origin of the coordinate system. A sphere with unit density, a diameter larger than the cube's side, and centered at the origin, was subtracted from the density function, causing its volume to intersect with the cube's faces. Although the image quality decreases as the number of projections is reduced, the shape remains distinctly recognizable even with a very limited number of projections, as few as 9 (Figure 8d).

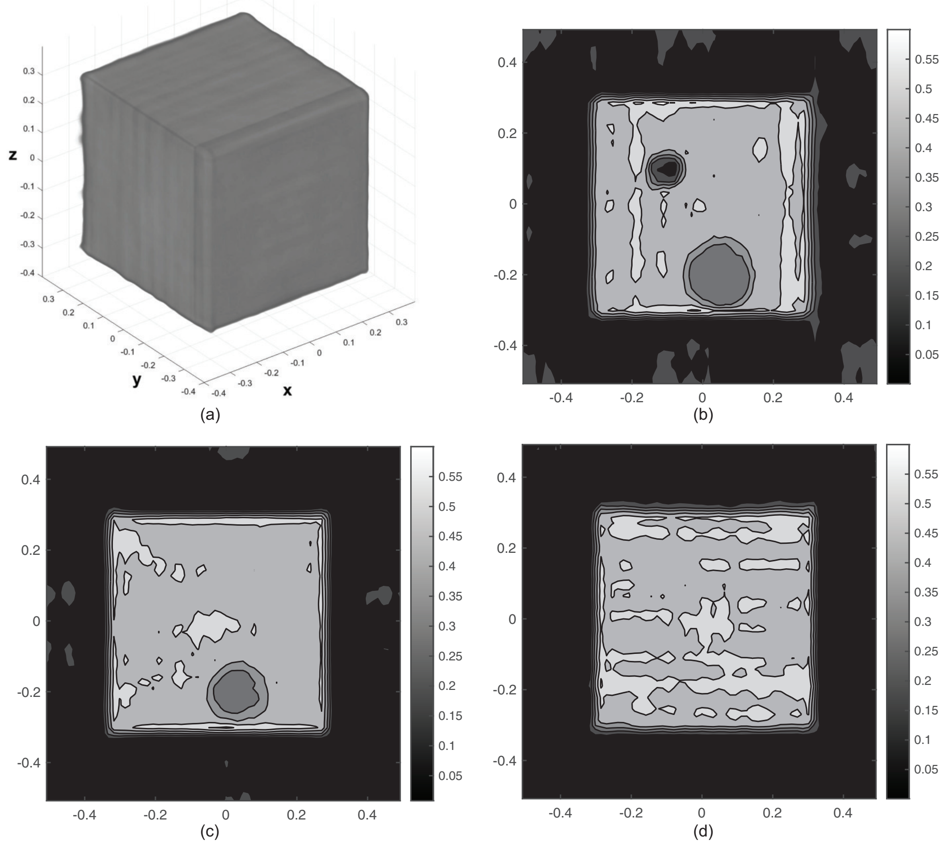

Figure 7: a) Reconstructed image, b) vertical cross section on the xz plane, c) vertical cross section on the yz plane, d) horizontal cross section on the xy plane.

4. 3D Reconstruction of light emission density in PROTO-SPHERA experiment

4.1. The PROTO-SPHERA experiment

PROTO-SPHERA (Spherical Plasma for HElicity Relaxation Assessment) is an innovative magnetic confinement plasma experiment aimed at advancing controlled thermonuclear fusion research. Its goal is to form plasma within a confined environment. Unlike tokamaks, where the plasma forms around a metal centerpost, in PROTO-SPHERA, the plasma forms around a plasma centerpost [3, 27, 31]. Tokamaks, the most extensively studied magnetic fusion configurations, have a non-simply connected geometry, where a central

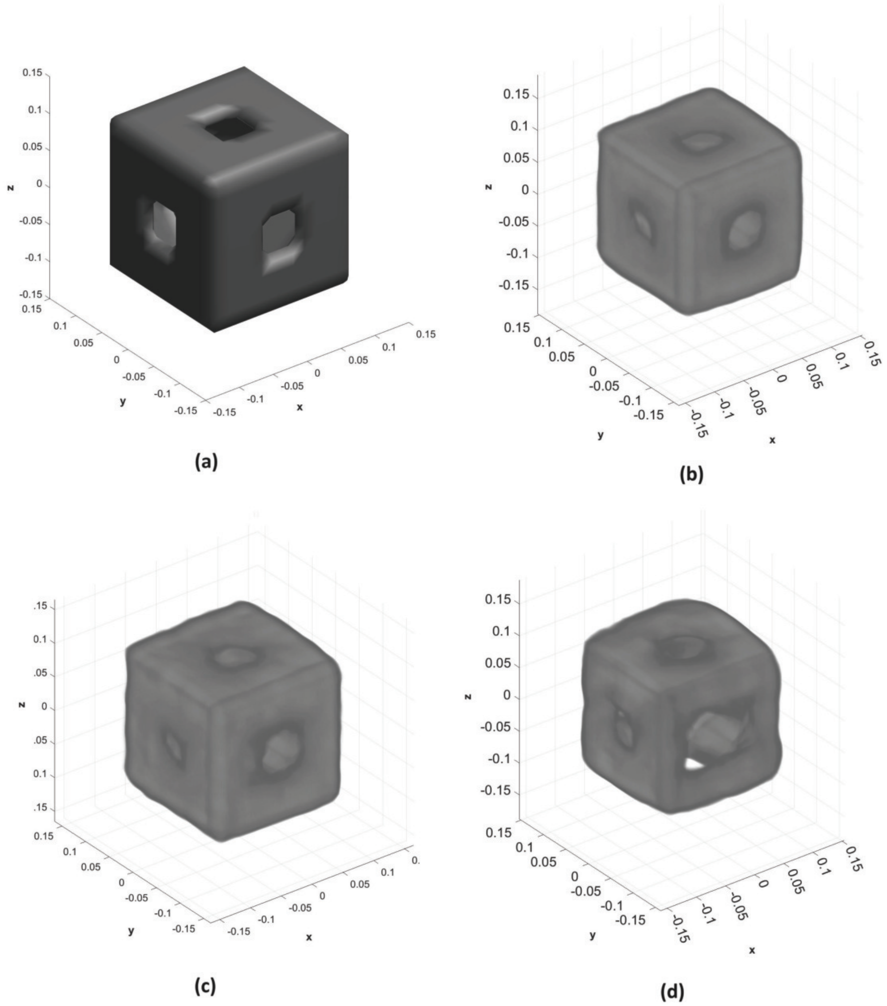

Figure 8: a) Source image and Reconstructed image with b) $12\times$, c) 6×6 and d) 3×3 projections.

post—containing the inner part of the toroidal magnet and the ohmic transformer—connects the plasma torus. The development of simply connected magnetic configurations relevant for fusion would significantly simplify the design of fusion reactors. Additionally, the PROTO-SPHERA experiment seeks to emulate astrophysical plasmas, such as jet and torus structures, in a laboratory setting [2].

Figure 9 shows a schematic of the PROTO-SPHERA experiment, which consists of a transparent cylindrical vacuum chamber measuring 2.5 meters in height and 2.0 meters in diameter, **held by a metal structure (Figure 9a)**. The vaccum chamber, surrounded by four columns, is equipped with electrodes at its ends and internal poloidal field coils (Figure 9b). The operating sequence proceeds as follows: the tungsten filaments of the cathode are heated to 2600-2900°C over 30 seconds, while the current in the poloidal field coils is ramped up to its final value. Gas is then introduced through a hollow section in the anode, reaching a pressure of 10^{-2} to 10^{-1} mbar, and a total voltage of 100-350 V is applied between the electrodes, yielding a centerpost current up to 10 kAmp. Under these conditions, **cold plasma with an energy in the range of 20-30 eV forms, with an emission concentrated in the visible and ultraviolet spectrum.**

To study the plasma formation process and the magneto-hydrodynamic phenomena occurring in the experiment, six high-speed cameras are positioned on the equatorial plane of the chamber, spaced 60 degrees apart (Figure 10). **It should be noted that in an ideal scenario free from errors, two cameras placed exactly 180 degrees apart would provide redundant information. However, real-world measurements are inevitably affected by several sources of error. These include, but are not limited to, slight misalignments in camera positioning, optical distortions, slight differences in vignetting due to material objects present inside the vessel, thermal expansion, structural vibrations, and electronic noise. In this context, having views from opposite sides of the plasma increases the robustness of the reconstruction and helps mitigate the effects of such errors**. Each camera has a resolution of 640x480 pixels and can capture 600 frames per second. Sample images recorded by the cameras at a specific time instant are shown in Figures 11a and 12a for shots with Helium and Hydrogen, respectively.

Combining the data from the cameras with measurements from a Langmuir probe has provided valuable insights into the dynamics of the plasma torus formation, including its size and emission spectrum. Numerous discharges were produced and observed throughout the experimental campaign.

The images captured by the six cameras are **assumed to be parallel projections onto vertical planes corresponding to the camera views** of the visible-light emission density, which plays the role of the density function f (Figures 11a and 12a). For each time instant, exploiting the corollary of the Fourier Slice Theorem of Section 3, these source images are

2D-Fourier transformed, then 3D-Fourier inverted to obtain the density of the visible light emitted by the plasma. The only change with respect to the procedure described in Section 3.2 is that, given the positioning of the cameras, the inversion has to be based on a cylindrical set of parallel projections instead of a spherical set, with ϕ fixed. Figures 11b and 12b show the reconstructed plasma light emission distribution derived from the images on the left for Helium and Hydrogen, respectively. It is important to note that the original images contain three layers of information, corresponding to the RGB color channels. The reconstructed images in Figures 11b and 12b are false-color representations, created by combining the RGB channels linearly with the following weighting: 100% Red, 86% Green, and 25% Blue [2].

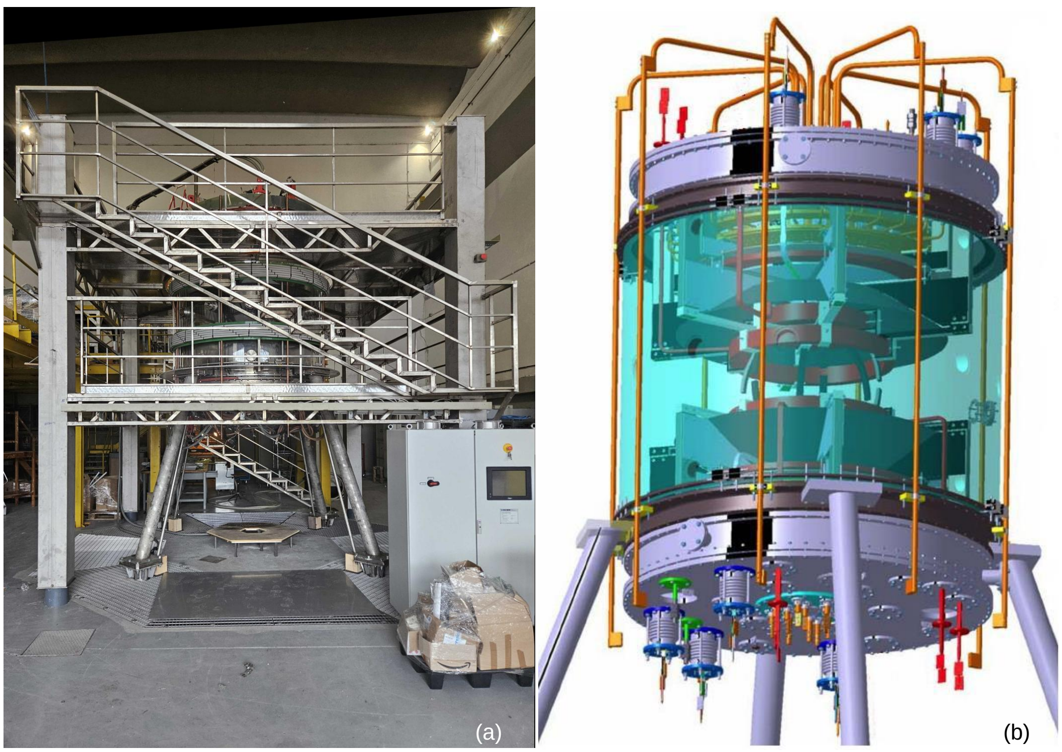

Figure 9: **a) Picture of PROTO-SPHERA setup and b) schematic of the machine**

4.2. Results and discussion

The proposed 3D tomography technique enabled detailed observation of the plasma torus formation process. The sequence begins with the formation

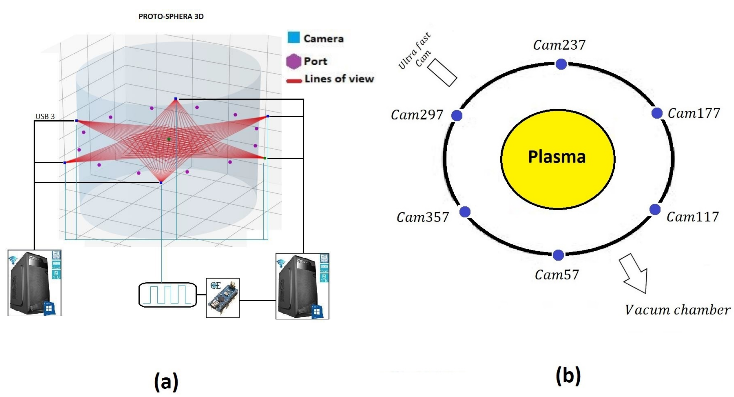

Figure 10: a) Position of the cameras in axonometry b) and plan

of a plasma column (pinch or centerpost) at a current lower than 10 kAmps. As the current reaches this value, the magnetic field lines bend, causing the pinch to become unstable, which leads to the formation of a torus around the centerpost. This progression is visualized in Figure 13 a-h, showing the reconstructed light emission density at eight sequential time steps (each 1/600 s apart) during a Helium plasma discharge. **These finding align closely with predictions from magnetohydrodynamic (MHD) models, in particular those presented in the work by García-Martínez et al. [16], whose magnetic field lines at different Lundquist numbers present a striking topological similarity with our emission density reconstruction (see Figure of 8 [16]).** The entire torus formation occurs within approximately 8 ms, five time steps intercurring from the arrangements of Figure 13 b to g. The presence of both jets and the torus strongly parallels astrophysical phenomena, as discussed in [2].

Once the spatial distribution of light emission density is known for each time instant, cross-sections can be derived, revealing further insights into plasma dynamics. Figure 14 shows an image of the Helium plasma captured by one of the six cameras (a) and a vertical cross-section (b) of the reconstructed light emission density in true color, taken at the same moment. To create this image, each of the three RGB channels was processed independently to generate a corresponding density function for each color. This cross-sectional view reveals the green color, which was obscured in the camera pictures by the intense orange glow of the 'ionization peel'—the layer between the plasma and the surrounding gas cushion. The correcness of the reconstruction is proved by the appearance of the Langmiur probe and of the copper bars on the right hand side of the picture. **These are external conducting copper bars (3 cm in diameter) that connect the two electrodes.**

Figure 15 presents vertical cross-sections of the plasma light emission density at the same time instants as Figure 13. These images further confirm the sequence of events leading to the formation of the torus, as described in the previous paragraph. Specifically, Figure 15 illustrates the emergence of a stable pinch (a-b), its progression towards instability (c-f), and ultimately the arrangement of the torus around the centerpost (d-h). Similar patterns, with comparable duration, were observed in other plasma discharges [2, 36]. Figure 16 presents a horizontal cross-section at the equatorial level, enabling observation of the same phenomena from a different perspective. In Figures 16d and 16e, the pinch's instability is particularly evident, as shown by the loss of axial symmetry and the presence of green regions on the right side of the images. **The phenomena described, featuring a centerpost around which a toroidal structure forms, show similar morphology with some theoretical results presented in [16], concerning MHD models, in particular, with those displaying the ratio between current density and magnetic field of an equatorial section. Further experimental confirmation of our finding comes from the PROTO-SPHERA research group, who obtained similar results using different reconstruction techniques. Specifically, Figure 17 reproduces a Figure of the work [9], and displays the plasma luminosity obtained through tomographic inversion using Zernike polynomials. The data in this figure refers to earlier experiments conducted with Argon gas and are shown in false colors. Data support the presence of the toroidal light emission structure and of the centerpost observed in our study. In the experiments reported in [9] not all the details of the setup had been finalized.**

Additionally, the horizontal cross-section analysis provides insights into plasma stability and torus thickness. Figure 18 illustrates selected horizontal cross-sections of Helium plasma at the equatorial level across sequential times, clearly depicting the torus encircling the centerpost. Notably, the light emission intensity varies over time, suggesting potential correlations with plasma density and stability. These images also allowed for the measurement of torus thickness, defined as the difference between the outer and inner circumferences' radii, which was observed to be between 0.25 and 0.35

m. **Note that, in Figure 18, the angle brilliance visible at the four corners is likey due to the reflection of light from the four metal columns supporting the vessel.** Similar behaviors were noted for Hydrogen plasma discharges, with an equatorial horizontal cross-section provided in Figure 19 for reference.

5. Conclusions

An imaging technique based on **a corollary of** the Fourier slice theorem was applied to reconstruct the light emission distribution of magnetically confined plasma in three dimensions. The **derived algorithm was used on pictures** capturing the visible light emission from Helium and Hydrogen plasmas, recorded by six cameras as part of the PROTO-SPHERA experiment at the ENEA Frascati laboratories. The results demonstrate that six images taken by cameras arranged in cylindrical symmetry enable an accurate 3D reconstruction of the plasma's spatial distribution at different time instants during the experiment. We observed that the plasma torus forms in approximately 8 ms, evolving from a kinked filament caused by the destabilization of the plasma centerpost. This 3D reconstruction allows for cross-sectional analysis, revealing previously hidden green light emission from the core, which had been obscured by the outer orange ionized layer. Additionally, equatorial cross-sections enabled the measurement of the torus thickness, which was found to range between 0.25 and 0.35 meters.

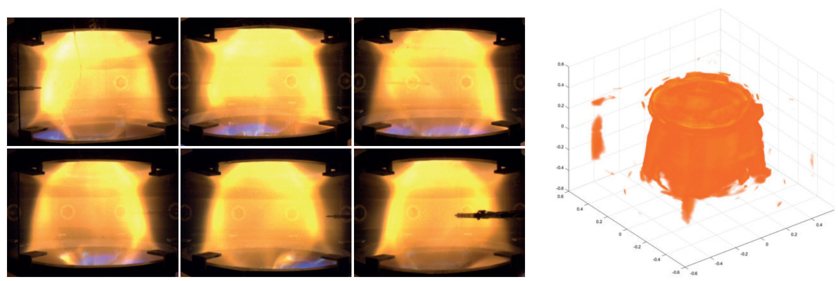

(a) (b)

Figure 11: a) Pictures recorded by the six cameras at a given time instant (267 msec) of the PROTO-SPHERA experiment from shot 2505 of Helium b) 3D reconstruction of plasma light emission density

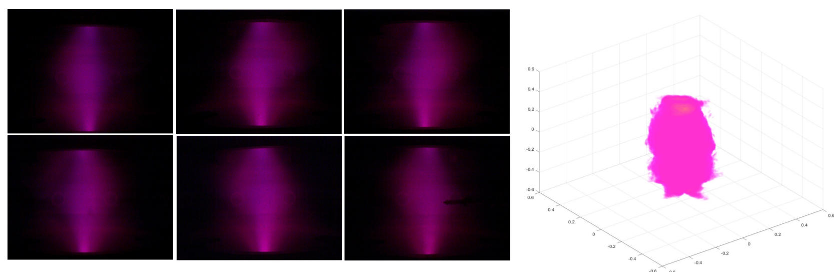

(a) (b)

Figure 12: a) Pictures recorded by the six cameras at a given time instant (233msec) of the PROTO-SPHERA experiment from shot 2154 of **Hydrogen** b) 3D reconstruction of plasma light emission density

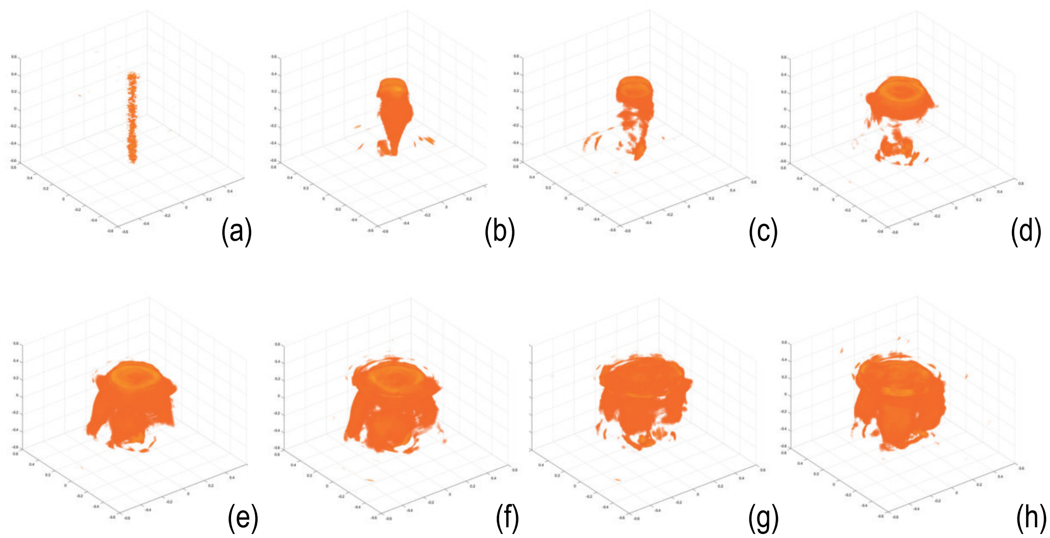

Figure 13: Reconstructed light emission density of Helium discharge 2505 at eight sequential time steps: stable pinch (a-b), pinch instability (c-f), formation of the plasma torus around the pintch (g-h)

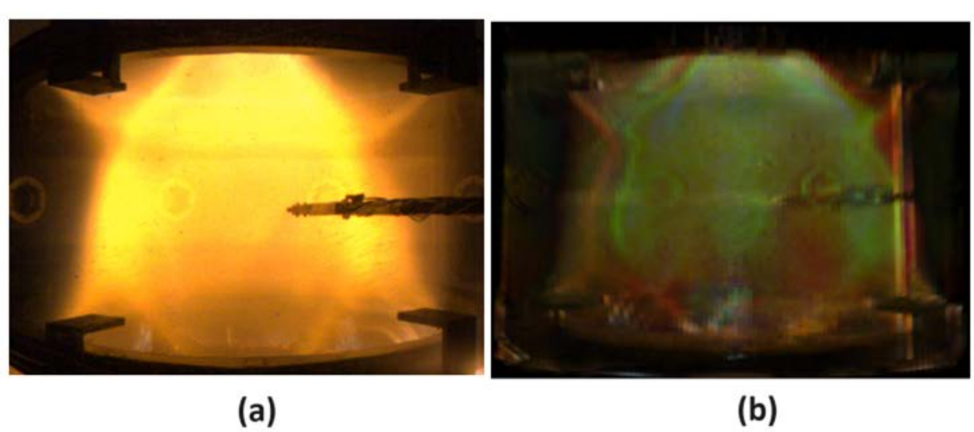

Figure 14: A projection of Helium plasma visible light emission captured by a camera during shot 2141 (a) and cross-section of the reconstructed light emission density in true colors (b).

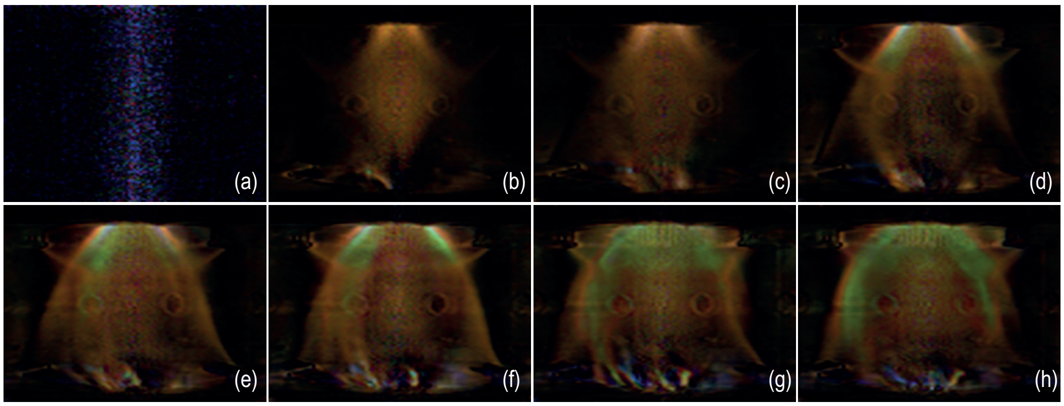

Figure 15: Vertical cross-sections of the reconstructed light emission density of Helium discharge 2505 at the same eight sequential time instants as Figure 12: stable pinch (a-b), pinch instability (c-f), formation of the plasma torus around the pinch (g-h)

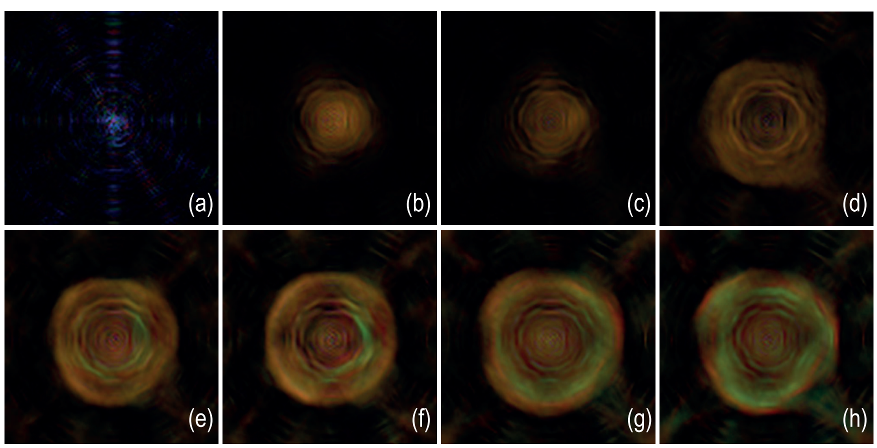

Figure 16: Horizontal cross-sections of the reconstructed light emission density of Helium discharge 2505 at the same eight sequential time instants as Figure 12: stable pinch (a-b), pinch instability (c-f), formation of the plasma torus around the pinch (g-h)

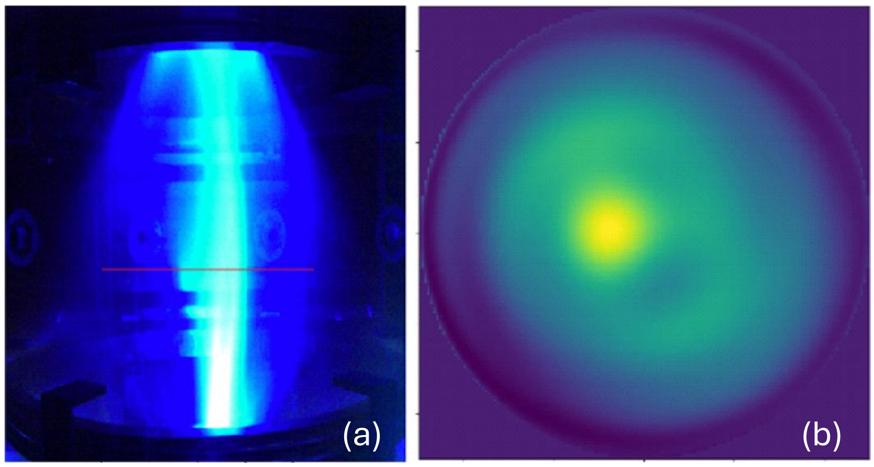

Figure 17: **Picture and related equatorial distribution of Argon plasma luminosity obtained by Zernike polynomials inversion [9]**

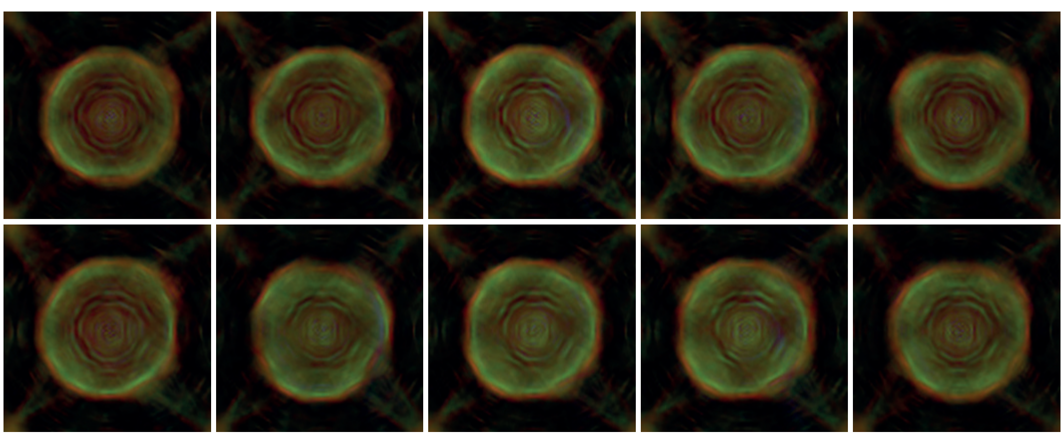

Figure 18: Sequence of reconstructed equatorial cross-sections of light emission density of Helium discharge 2505 at 10 time instants

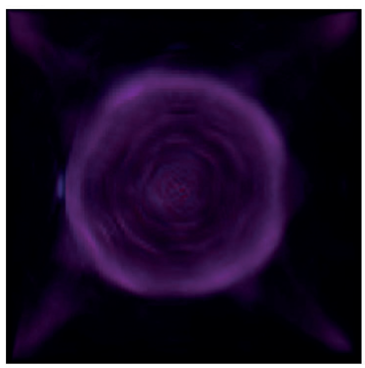

Figure 19: Equatorial cross-section of light emission density of **Hydrogen** discharge 2154

References

[1] Amir M. Alani, Francesco Soldovieri, Ilaria Catapano, Iraklis Giannakis, Gianluca Gennarelli, Livia Lantini, Giovanni Ludeno, and Fabio Tosti. The use of ground penetrating radar and microwave tomography for the detection of decay and cavities in tree trunks. *Remote Sensing*, 11(18), 2019.

[2] F. Alladio, P. Micozzi, L. Boncagni, A. Pau, S. Naghinajad, S. Macera, Y. Damizia, P. Buratti, F. Filippi, G. Galatola Teka, F. Giammanco, E. Giovannozzi, M. Iafrati, A. Lampasi, and P. Marsili. PROTO-SPHERA: a magnetic confinement experiment which emulates the jet + torus astrophysical plasmas. *Plasma Physics and Controlled Fusion*, 66(3), 2024.

[3] Franco Alladio, Paolo Costa, Alessandro Mancuso, Paolo Micozzi, Stamos Papastergiou, and Francois Rogier. Design of the PROTO-SPHERA experiment and of its first step (MULTI-PINCH). *Nuclear Fusion*, 46:S613–S624, 2006.

[4] Habib Ammari. Tomographic imaging with non-diffracting sources. an introduction. *Mathematics of Emerging Biomedical Imaging*, 28(10):95–106, 2008.

[5] Amir Averbuch and Yoel Shkolnisky. 3D Fourier based discrete Radon transform. *Applied and Computational Harmonic Analysis*, 15(1):33 – 69, 2003.

[6] T. Buzug. ***Computed Tomography***. Springer: Berlin, Heidelberg, 2008.

[7] V. Cnudde and M.N. Boone. High-resolution X-ray computed tomography in geosciences: A review of the current technology and applications. *Earth-Science Reviews*, 123:1 – 17, 2013.

[8] A. M. Cormack. Early two-dimensional reconstruction and recent topics stemming from it. *Science*, 209:1482–1486, 1980.

[9] Yacopo Damizia, Matteo Iafrati, Davide Liuzza, Luca Boncagni, Paolo Micozzi, and Franco Alladio. **Optical tomography of the plasma**

on the PROTO-SPHERA experiment. *Fusion Engineering and Design*, 169, 2021.

[10] L. De Chiffre, S. Carmignato, J.-P. Kruth, R. Schmitt, and A. Weckenmann. Industrial applications of computed tomography. *CIRP Annals - Manufacturing Technology*, 63(2):655 – 677, 2014.

[11] S.R. Deans. *The Radon Transform and some of its applications*. Wiley: New York, 1983.

[12] Musa Sani Musa Niyazi Şentürk Fatih Veysel Nurçin Dilber Uzun Ozsahin, Berna Uzun and Ilker Ozsahin. Evaluating nuclear medicine imaging devices using fuzzy PROMETHEE method. *Procedia computer science*, 120:699–705, 2017.

[13] S. Donato, L. Brombal, L.M. Arana Peña, F. Arfelli, A. Contillo, P. Delogu, F. Di Lillo, V. Di Trapani, V. Fanti, R. Longo, P. Oliva, L. Rigon, L. Stori, G. Tromba, and B. Golosio. Optimization of a customized simultaneous algebraic reconstruction technique algorithm for phase-contrast breast computed tomography. *Physics in Medicine and Biology*, 67(9), 2022.

[14] Mario D'Acunto, Antonio Benassi, Davide Moroni, and Ovidio Salvetti. 3D image reconstruction using Radon transform. *Signal, Image and Video Processing*, 10(1):1 – 8, 2016.

[15] Jeffrey Fessler. Optimization methods for magnetic resonance image reconstruction: Key models and optimization algorithms. *IEEE signal processing magazine*, 37(1):33–40, 2020.

[16] Pablo Luis García-Martínez, Leandro Gabriel Lampugnani, and Ricardo Farengo. Effect of the helicity injection rate and the Lundquist number on spheromak sustainment. *Physics of Plasmas*, 21(12), 2014.

[17] Richard Gordon, Robert Bender, and Gabor T. Herman. Algebraic reconstruction techniques (ART) for three-dimensional electron microscopy and X-ray photography. *Journal of Theoretical Biology*, 29(3):471–476,IN1–IN2,477–481, 1970.

[18] David Gottlieb, Bertil Gustaffson, and Patrick Forssen. On the direct Fourier method for computed tomography. *IEEE Transactions on Medical Imaging*, 19(3):223–232, 2000.

[19] R.S. Granetz and P. Smeulders. **X-ray tomography on JET**. *Nuclear Fusion*, 28(3):457 – 476, 1988.

[20] B Gustaffson. Mathematics for computed tomography. *Physica Scripta*, T61:38– 43, 1996.

[21] G. N. Hounsfield. Computerized transverse axial scanning (tomography): Part I. description of system. *British Journal of Radiology*, 46(3):1016–1022, 1973.

[22] P. Huthwaite. Guided wave tomography with an improved scattering model. *Proceedings of the Royal Society A: Mathematical, Physical and Eng. Sciences*, 472(2195), 2016.

[23] A. Jardin, J. Bielecki, D. Mazon, Y. Peysson, K. Król, D. Dworak, and M. Scholz. **Implementing an X-ray tomography method for fusion devices**. *European Physical Journal Plus*, 136(7), 2021.

[24] A. C. Kak and M. Slaney. *Principles of Computerized Tomographic Imaging*. IEEE press, 1988.

[25] Avinash C. Kak. Computerized tomography with X-ray, emission, and ultrasound sources. *Proceedings of the IEEE*, 67(9):1245 – 1272, 1979.

[26] Mohd Taufiq Mohd Khairi, Sallehuddin Ibrahim, Mohd Amri Md Yunus, M. Faramarzi, Goh Pei Sean, Jaysuman Pusppanathan, and A. Abid. Ultrasound computed tomography for material inspection: Principles, design and applications. *Measurement: Journal of the International Measurement Confederation*, 146:490 – 523, 2019.

[27] Alessandro Lampasi, Giuseppe Maffia, Franco Alladio, Luca Boncagni, Federica Causa, Edmondo Giovannozzi, Luigi Andrea Grosso, Alessandro Mancuso, Paolo Micozzi, Valerio Piergotti, Giuliano Rocchi, Alessandro Sibio, Benedetto Tilia, and Vincenzo Zanza. Progress of the plasma centerpost for the PROTO-SPHERA spherical tokamak. *Energies*, 9(7), 2016.

[28] Xin Li, Yudong Lu, Xiaozhou Zhang, Wen Fan, Yangchun Lu, and Wangsheng Pan. Quantification of macropores of malan loess and the hydraulic significance on slope stability by x-ray computed tomography. *Environmental Earth Sciences*, 78(16), 2019.

[29] E. Maire and P.J. Withers. Quantitative X-ray tomography. *Int. Materials Reviews*, 59(1):1 – 43, 2014.

[30] Francisco A. Matos, Diogo R. Ferreira, and Pedro J. Carvalho. **Deep learning for plasma tomography using the bolometer system at JET**. *Fusion Engineering and Design*, 114:18 – 25, 2017.

[31] Paolo Micozzi, Franco Alladio, Alessandro Mancuso, Vincenzo Zanza, Gerarda Apruzzese, Francesca Bpmbarda, Luca Boncagni, Paolo Buratti, Francesco Filippi, Giuselle Galatola Teka, Francesco Giammarco, Edmondo Giovannozzi, Andrea Grosso, Matteo Iafrati, Alessandro Lampasi, Violeta Lazic, Simone Magagnino, Simone Mannori, Paolo Marsili, Paolo Piergotti, Giuliano Rocchi, Alessandro Sibio, Benedetto Tilia, and Onofrio Tudisco. Final results of the first phase of the PROTO-SPHERA experiment: obtainment of the full current stable screw pinch and first evidences of the jet + torus combined plasma configurationy. *Plasma Science and Technology*, 26:025103, 2024.

[32] Jan Mlynar, Teddy Craciunescu, Diogo R. Ferreira, Pedro Carvalho, Ondrej Ficker, Ondrej Grover, Martin Imrisek, and Jakub Svoboda. **Current Research into Applications of Tomography for Fusion Diagnostics**. *Journal of Fusion Energy*, 38(3-4):458 – 466, 2019.

[33] M. Odstrcil, J. Mlynar, T. Odstrcil, B. Alper, and A. Murari. **Modern numerical methods for plasma tomography optimisation**. *Nuclear Instruments and Methods in Physics Research, Section A: Accelerators, Spectrometers, Detectors and Associated Equipment*, 686:156 – 161, 2012.

[34] Tugba Ozge Onur. An application of filtered back projection method for computed tomography images. *International Review of Applied Sciences and Engineering*, 12(2):194 – 200, 2021.

[35] Yongwoo Park, Un-Chul Paek, and Dug Young Kim. Characterization of a stress-applied polarization-maintaining (PM) fiberthrough photoe-

lastic tomography. *Journal of lightwave technology*, 21(4):997 – 1004, 2003.

[36] A. Pau, S. Naghinajad, F. Alladio, P. Micozzi, and L. Boncagni. 3D tomography of Hydrogen and Helium plasma produced in th PROTO-SPHERA experiment. In *Proceedings of the ASME 2024 51st Annual Review Progress in Quantitative Nondestructive Evaluation QNDE2024*, pages 1–7, Denver, Colorado, July 2024.

[37] Johann Radon. On the determination of functions from their integral values along certain manifolds (translation from the original German text published in Berichte der Sächsischen Akademie der Wissenschaft, vol. 69, pp. 262-277, 1917). *IEEE Transactions on Medical Imaging*, MI-5(4):170–176, 1986.

[38] L. Schoeman, P. Williams, A. du Plessis, and M. Manley. X-ray micro-computed tomography (μCT) for non-destructive characterisation of food microstructure. *Trends in Food Science and Technology*, 47:10 – 24, 2016.

[39] James Anthony Seibert. Iterative reconstruction: how it works, how to apply it. *Pediatric Radiology*, 44(3):431 – 439, 2014.

[40] Wolfram Stiller. Basics of iterative reconstruction methods in computed tomography: A vendor-independent overview. *European Journal of Radiology*, 109:147 – 154, 2018.

[41] M.L.L. Wijerathne, Kenji Oguni, and Muneo Hori. Tensor field tomography based on 3D photoelasticity. *Mechanics of Materials*, 34(9):533 – 545, 2002.

[42] Tao Zhang, Yuxiang Xing, Li Zhang, Xin Jin, Hewei Gao, and Zhiqiang Chen. Stationary computed tomography with source and detector in linear symmetric geometry: Direct filtered backprojection reconstruction. *Medical physics*, 47(5):2222–2236, 2020.

[43] Yingying Zhang-O'Connor and Jeffrey A. Fessler. Fourier-based forward and back-projectors in iterative fan-beam tomographic image reconstruction. *IEEE Transactions on Medical Imaging*, 25(5):582 – 589, 2006.

[44] Dominique Zosso, Benoît Le Callennec, Meritxell Bach Cuadra, Kamiar Aminian, Brigitte M. Jolles, and Jean-Philippe Thiran. Bi-planar 2D-to-3D registration in fourier domain for stereoscopic X-ray motion tracking. volume 6914, 2008.

3D tomographic reconstruction of light emission density of plasma in the PROTO-SPHERA experiment

Shayesteh Naghinajad[a], Franco Alladio[b], Paolo Micozzi[c], Luca Boncagni[c]

[a] *Department of Structural and Geotchnical Engineering, Sapienza University of Rome, via Eudossiana 18, 00184 Roma, Italy*
[b] *INAF-IAPS National Institute of Astrophysics, Via del Fosso del Cavaliere 100, 00133 Roma, Italy*
[c] *Nuclear Research Department, ENEA Italian National Agency for Technology, Energy and Sustainable Economic Development Via Enrico Fermi 45, 00044 Frascati (RM), Italy*

Abstract

We address a key challenge in plasma diagnostics: reconstructing the three-dimensional (3D) light emission density from projection data. To this end, we employ a method for reconstructing 3D density functions based on a corollary of the 3D Fourier slice theorem. This corollary establishes a connection between 2D plane projections and plane sections of the 3D Fourier transform, enabling a direct and non-iterative solution to the inverse problem. The method is applied to the PROTO-SPHERA experiment, an innovative magnetic confinement plasma setup for controlled nuclear fusion research. Experimental data were acquired using six high-speed cameras arranged with cylindrical symmetry around the plasma chamber, capturing time-resolved pictures that are assumed to be parallel projections of the visible light emissions from Helium and Hydrogen discharges. After a transformation of coordinates, by computing their inverse 3D Fourier transform, we reconstruct the spatial distribution of light emission density. This technique enabled to reveal dynamic features of plasma self-organization—such as torus formation around a centerpost—and provides internal cross-sectional views of the plasma, displaying previously obscured spectral components.

Email addresses: `annamaria.pau@uniroma1.it` (), `shayesteh.naghinajad94@gmail.com` (Shayesteh Naghinajad), `franco.alladio@protosphera.it` (Franco Alladio), `paolo.micozzi@enea.it` (Paolo Micozzi), `luca.boncagni@enea.it` (Luca Boncagni)

Keywords: 3D image reconstruction, magnetically confined plasma, nuclear fusion, monitoring

---

1. Introduction

Tomographic computed (CT) imaging or scanning is a technique of data treatment which enables visualization of the inner part of objects instead of making real cuts. This has obvious and important applications in the medical field, as well as in the nondestructive monitoring of structures and industrial processes. CT requires the solution of an inverse problem, which can be formulated as follows: given the knowledge of some data called projections, reconstruct the spatial distribution of a density function $f(x, y, x)$ which represents some property (for instance mass density) of an object in the 3D space. Projections are obtained by illuminating the object with stimuli which produce a measurable response, which is measured on the object boundary. Projections are, in practice, a sort of shade that the function $f(x, y, x)$ projects onto lines, or planes. The mathematical demonstration that a density function could be reproduced from an infinite set of its projections was provided by the mathematician J. Radon [37] at the beginning of last century. However, it is quite remarkable that reconstruction of images from projections was not attempted until 1940. In 1972, Hounsfield [21] proposed the first method that allowed to image plane slices of the internal structure of a human body using X-rays projections. The Nobel prize in physiology and medicine in 1979 awarded to Hounsfield and Cormack [8] for their work on the initial computed tomography device signifies the importance that this technique has in the medical field. Since then, the use of computed tomography was extended to a wide number of industrial applications [10], among which food industry [38], materials science [29], geosciences [7] and fusion diagnostics [19, 33, 30, 32].

Medical and industrial computed tomography is based on the same underlying principles but differs in the acquisition system layout, as well as in the stimulus that is used to obtain the projections, which is X-rays in medical CT, but can also be another physical source. In fact, the reflected or transmitted signal of any source which produces a measurable response of the scanned object can be used. The feasibility of using ultrasounds [25, 22, 26], the photo elastic effect [41], or even ground-penetrating radar emitting microwaves [1] has been proved to be effective to visualize internal patterns of objects. Different sources interact with different properties, which can include, besides mass density, electrical, acoustic, and electromagnetic properties of materials and tissues. For instance, in nuclear medicine, the interest is focused on reconstructing a cross-sectional image of radioactive isotope distributions within the human body [12], while in magnetic resonance the magnetic properties of the object is reconstructed [15]. The photelastic effect instead was used to determine the plane stress distribution in an optical fiber [35]. The most fundamental distinction between medical CT and fusion diagnostics lies in the nature of the signal: while medical tomography is primarily concerned with absorption, fusion diagnostics focuses on emission. The main difference between the mentioned sources is that some of them are non-diffracting, like X-rays, which travel in straight lines [4], while some others are diffracting, like ultrasounds, that is, they are scattered in all directions, resulting in a more complex inverse problem [24].

To convert the measured response data into an image, appropriate processing is necessary. The most popular algorithms that are in use can be classified into two major categories, which are iterative and analytical methods [20]. Iterative methods are numerical reconstruction algorithms that employ a model to predict the measured data from an initial estimate and then refine the image estimate to better fit the measured data. This process is repeated iteratively until the image quality meets a predetermined standard or until further iterations do not significantly change the image [39, 40]. Starting from the Algebraic Reconstruction Technique (ART) [17], research continues to evolve with refinements and developments, such as the customized Simultaneous Algebraic Reconstruction Technique (SART) [13], and the Simultaneous Iterative Reconstruction Technique (SIRT) [42]. Analytical algorithms are based on mathematical models and explicit formulas that directly compute the image from the acquired projection data. They can be further categorized into two groups: the direct or Fourier-Transform-based methods [43, 18] and the Back-Projection-based algorithms, like Simple Back Projection (SBP), Linear Back Projection (LBP) and Filtered Back Projection (FBP) [34, 42]. Fourier-Transform-based algorithms rely on the relationship between the Fourier transform (FT) of the image and the Fourier transform of its projections. More specifically, projections are obtained using Radon transforms [24], that is by computing line integrals of the density function. A more detailed discussion of the literature on the classification of CT algorithms is beyond the scope of this paper. The interested reader can consult [26, 11] for a more eshaustive presentation of the matter.

2. Application of tomography to fusion diagnostics

In tokamaks, reconstruction of X-ray emission relies on data collected by line-integrated detectors — such as pinhole X-ray cameras, bolometers, and neutron cameras— arranged across a cross-section of the plasma. Unlike medical imaging systems, which benefit from unrestricted access to the subject from all angles, fusion diagnostics is constrained by the geometry of the tokamak. The number and placement of detectors are limited by the physical design of the device, leading to a much lower spatial resolution than that achievable in medical tomography. As a consequence of this sparse and uneven data, plasma tomography requires additional assumptions, such as smoothness or regularity of the emission field, regardless of the inversion technique employed [23].

Under these circumstances, analytical and iterative methods faced various challenges, prompting the development of dedicated numerical techniques specifically tailored for 2D cross-sectional plasma tomography. These numerical approaches rely on an algebraic formulation of the image reconstruction problem, where each equation represents the equality between a known measured integral and the sum of emissions along a corresponding line of sight. However, the resulting system is typically underdetermined and the problem ill-posed, with high sensitivity to data error. To address this issue, various regularization techniques are employed to constrain the solution space, often by promoting smoothness or limiting complexity in the results. Among the robust regularization methods used in plasma tomography, Tikhonov regularization, Maximum Likelihood estimation, and Fisher information-based approaches are particularly noteworthy [32, 30]. In addition, there have been efforts to apply neural networks and deep learning techniques to tomographic reconstruction, offering promising alternatives for handling the inherent challenges of the problem [33].

In this work, we aim to apply tomographic techniques to reconstruct the light emission density recorded during the PROTO-SPHERA experiment deployment [2], conducted at the ENEA laboratories (Italian National Agency for New Technologies, Energy and Sustainable Development) in Frascati, Italy. During the experiment, the plasma emits photons, whose light is captured by six cameras arranged with cylindrical symmetry. PROTO-SPHERA is an innovative magnetic confinement plasma experiment designed for research in controlled thermonuclear fusion. Its goal is to form a plasma torus not around a solid metal centerpost, as in traditional tokamaks, but around a plasma centerpost. This setup introduces significant differences compared to the reconstruction of X-ray emission density in tokamaks. Firstly, PROTO-SPHERA provides unobstructed visual access from any viewing angle. Secondly, the plasma produced by PROTO-SPHERA has emission concentrated in the visible and ultraviolet spectrum. Last but not least, the optical system uses lenses, producing a sharp image with limited perspective effect, due to the distance between plasma and cameras. The image that can then be treated as a parallel projection of light emission.

To the best of our knowledge, fusion plasma tomography, was only carried out on sections of the torus. Here, we employ the imaging technique based on a corollary to Fourier slice theorem in 3D, also called Fourier Section Theorem [6, 44] and based on an nth-dimension formulation of the Radon transform, provided by Radon himself: by calculating 3D inverse Fourier transforms of 2D Fourier transforms of plane projections, the 3D image of the scanned object can be reconstructed. This differs from the classical tomographic approach [28, 14], where a 3D image is reconstructed by assembling stacks of images deriving from of reconstructed images on several parallel planes. This work represents a first step toward 3D reconstruction of the plasma visible light emission density, which has never been attempted before. The resulting images enabled the observation of important aspects of plasma formation and arrangement.

This paper is organized into two sections: Section 3 revises the method of image reconstruction in 3D based on a corollary of the Fourier slice theorem, and Section 4 reports the experimental results. For the ease of the reader, in Subsection 3.1, the 3D continuous Radon transform is recalled, then in Subsection 3.2 the lemma of the Fourier slice theorem that is at the base of the image reconstruction method employed is presented. In Subsection 3.3 proof of the effectiveness of the reconstruction method is provided by using numerical data. Subsection 4.1 describes the PROTO-SPHERA experiments, and Subsection 4.2 illustrates how the tomographic reconstruction enabled to prove the sustainment of the plasma torus around the centerpost and provided further useful information on the dynamics of confined plasma.

3. Analytical direct 3D image reconstruction

3.1. 3D continuous Radon Transform

For simplicity's sake, the 2D Radon transform is first introduced. Let us consider a plane object - or a slice of a 3D object - with density function

$f(x,y)$ (Figure 1). Its projections onto a line inclined by an angle θ with respect to the x axis are obtained by integrating $f(x,y)$ on the set of parallel lines (rays) that are inclined by an angle $\theta+\pi/2$ with respect to the x axis and at a distance t from the origin of the coordinate system (bold line in Figure 1). The equation of a ray is:

$$t = x\,cos\theta + y\,sin\theta. \tag{1}$$

The projection of the function $f(x,y)$ is then defined as:

$$p(\theta,t) = \int_{-\infty}^{\infty}\int_{-\infty}^{\infty} f(x,y)\delta(x\,cos\theta + y\,sin\theta - t)dxdy, \tag{2}$$

where δ is the Dirac's delta function. Equation (2) represents the 2D continuous Radon transform $[\mathcal{R}_2 f](\theta,t)$ of the function f, which is depicted schematically in Figure 1 by the blue curve subtending the sky blue area. It is often preferred to integrate in the rotated coordinate system (t,s), where the projection can be written as:

$$p(\theta,t) = \int_{-\infty}^{\infty} f(t,s)ds. \tag{3}$$

Geometrically, the continuous 2D Radon transform maps a function in $\mathbb{R}^2$ into the set of its line integrals in $\mathbb{R}^2$. The reconstructed image function $f(x,y)$ is formally obtained by inverting the Radon transform:

$$f(x,y) = [\mathcal{R}_2^{-1} p](\theta,t). \tag{4}$$

Let us now consider a 3D object with density function $f(x,y,z)$ (Figure 2). Its projections are obtained by integrating $f(x,y,z)$ on the plane Σ that is orthogonal to the versor $\boldsymbol{\alpha}$ and at a distance d from the origin of the coordinate system. The versor has direction cosines $\boldsymbol{\alpha} = (cos\theta\,cos\phi, sin\theta\,cos\phi, sin\,\phi)^T$, where ϕ is the angle that $\boldsymbol{\alpha}$ forms with the z axis, and θ is the angle that the projection of $\boldsymbol{\alpha}$ onto the xy plane forms with the x axis. The equation of a plane orthogonal to $\boldsymbol{\alpha}$ and at a distance d from the origin is:

$$d = x\,cos\theta\,cos\phi + y\,sin\theta\,cos\phi + z\,sin\phi. \tag{5}$$

In an analogy with Equation (2), the projection of the function $f(x,y,z)$ associated with the couple $(\boldsymbol{\alpha}, d)$ is then defined as:

$$p(\boldsymbol{\alpha}, d) = \int_{-\infty}^{\infty}\int_{-\infty}^{\infty}\int_{-\infty}^{\infty} f(x,y,z)\delta(x\, cos\theta\, cos\phi + y\, cos\theta\, sin\phi + z\, sin\theta - d)dxdydz. \tag{6}$$

The area over which the previous integral is computed is included in the dashed line in Figure 2. Equation (6) represents the 3D continuous Radon transform $[\mathcal{R}_3 f](\boldsymbol{\alpha}, t)$ of the function f. Geometrically, the continuous 3D Radon transform maps a function in $\mathbb{R}^3$ into the set of its plane integrals in $\mathbb{R}^3$. The reconstructed image function $f(x, y, z)$ is formally obtained by inverting the Radon transform:

$$f(x, y, z) = [\mathcal{R}_3^{-1} p](\boldsymbol{\alpha}, d). \tag{7}$$

It is important to note that in real applications we won't be dealing with plane integrals. In fact, $\mathcal{R}_3$ can be obtained by computing the $\mathcal{R}_2$ of the intersection

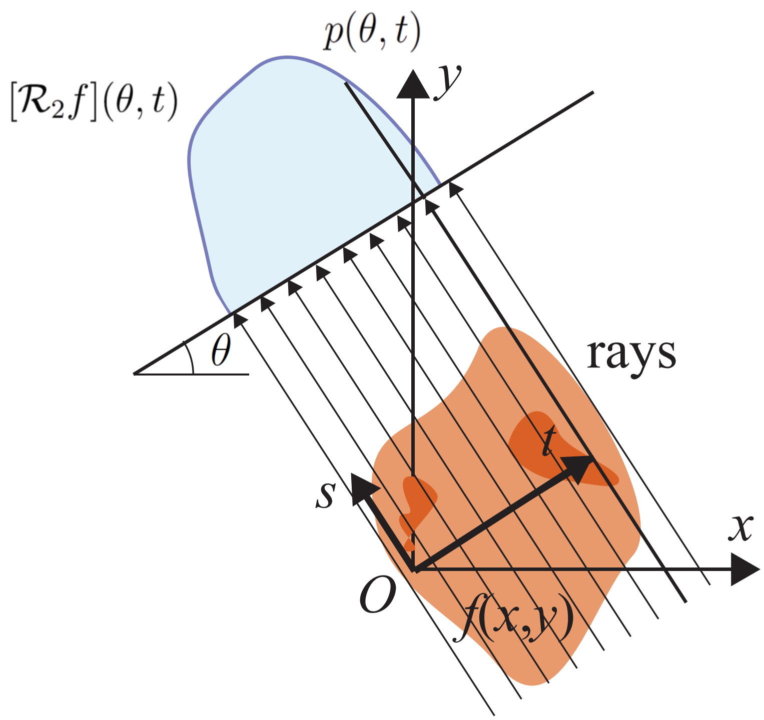

Figure 1: Projection of a plane density function onto a line.

between f and the plane Σ, and then integrating over lines orthogonal to the rays, which are displayed in Figure 3 as yellow lines. The line integrals are much easier to be obtained in practical measurements. They correspond to projections onto detector planes taken from different angles, or, in the present case, to pictures taken from different cameras.

With the definition introduced above, the detector plane still has a rotational degree of freedom around the detector normal. Different from what is done in [6], here we integrate in the rotated coordinate system (t, s, r), whose axes t and s coincide with the tangent lines to the parallels and meridians, respectively, of an imaginary sphere centered in the origin of the system of coordinates, at the point of intersection between the sphere and the versor $\boldsymbol{\alpha}$, with the orientation of the r axis coinciding with that of $\boldsymbol{\alpha}$ (Figure 3, upper left). The plane (t, s) is the detector plane. The transformation of coordinates from (x, y, z) to (t, s, r) can be written as:

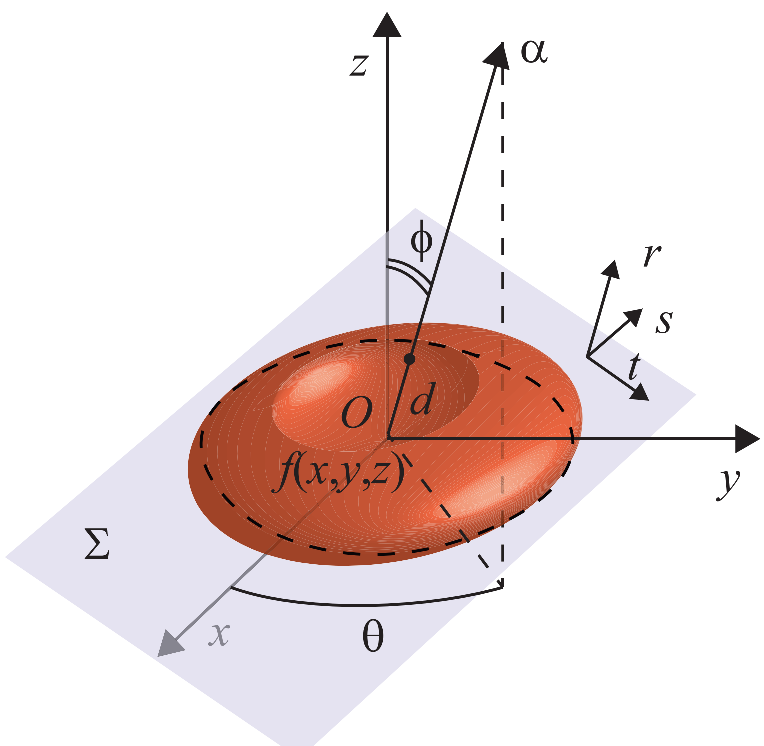

Figure 2: Projection of a 3D density function onto a plane.

$$\begin{bmatrix} t \\ s \\ r \end{bmatrix} = \begin{bmatrix} cos\phi & 0 & sin\phi \\ 0 & 1 & 0 \\ sin\phi & 0 & cos\phi \end{bmatrix} \begin{bmatrix} cos\theta & sin\theta & 0 \\ -sin\theta & cos\theta & 0 \\ 0 & 0 & 1 \end{bmatrix} \begin{bmatrix} x \\ y \\ z \end{bmatrix}. \tag{8}$$

Moreover, the distance d can be expressend in the (t, s, r) system of coordinates as $d = \sqrt{t^2 + r^2}$. The ray integral is then expressed as follows:

$$p(\theta, \phi, t, r) = \int_{-\infty}^{\infty} f(t, s, r) ds. \tag{9}$$

The integral $p(\theta, \phi, t, r)$ is in practice a line projection of the 3D function. The set of all the line projections on the plane (t, r) for given θ and ϕ will be denoted as $P_{\theta,\phi}$.

3.2. 3D Fourier slice theorem

The extension of the Fourier slice theorem to higher dimensions, enables direct reconstruction of 3D objects. The 3D Fourier Slice Theorem can be stated as follows.

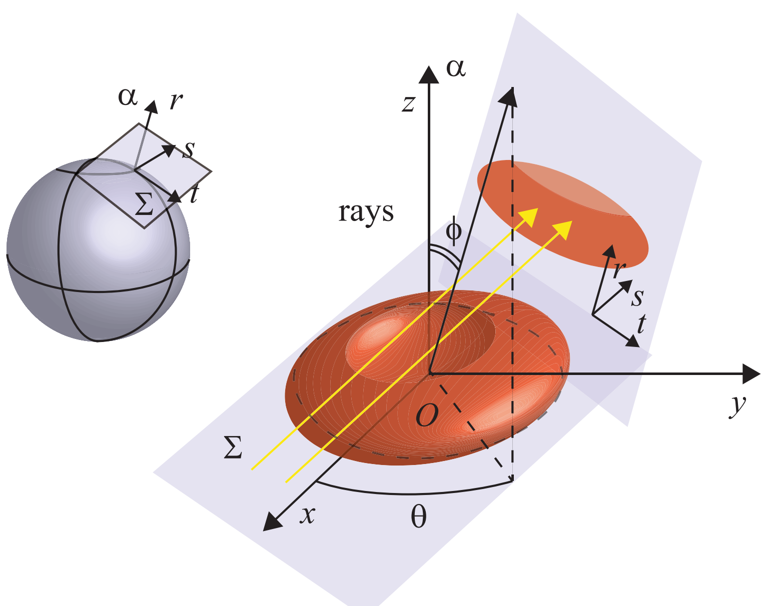

Figure 3: Ray integrals over a 3D function.

Theorem 1. *A line slice of the 3D Fourier transform of the function $f(x, y, z)$ equals the 1D Fourier Transform of the 3D Radon transform $[\mathcal{R}_3 f](\boldsymbol{\alpha}, t)$ at the same angle.*

For proof, the interested reader can consult [44, 5]. However, the theorem in this form is of little use for practical purposes. A useful corollary can be stated. See for instance [6].

Corollary 1.1. *A plane slice of the 3D Fourier transform of the density function $f(x, y, z)$ equals the 2D Fourier Transform of the set of line projections at the same angle.*

Proof. Let us consider the line projection of a 3D density function $P_{\theta,\phi}$, and take its 2D Fourier Transform ($\mathcal{F}_2$):

$$[\mathcal{F}_2 P_{\theta,\phi}](\mu, \nu) = \int_{-\infty}^{\infty} \int_{-\infty}^{\infty} P_{\theta,\phi}(t, r) e^{-2\pi i(\mu t+\nu r)} dtdr, \tag{10}$$

where μ and ν are the wavenumbers in the t, r directions, respectively and i is the imaginary unit.
By substituting equation (9) into equation (10), we get:

$$[\mathcal{F}_2 P_{\theta,\phi}](\mu, \nu) = \int_{-\infty}^{\infty} \int_{-\infty}^{\infty} [\int_{-\infty}^{\infty} f(t, s, r) ds] e^{-2\pi i(\mu t+\nu r)} dtdr. \tag{11}$$

Based on the transformation (8), the rotated coordinate system (t, s, r) can be converted back into the initial (x, y, z) system:

$$\begin{aligned} [\mathcal{F}_2 P_{\theta,\phi}](\mu, \nu) &= \int_{-\infty}^{\infty} \int_{-\infty}^{\infty} \int_{-\infty}^{\infty} f(x, y, z)\, e^{-2\pi i k}\, dx\, dy\, dz \\ \text{with} \quad k &= \mu \cos\phi \cos\theta\, x + \mu \cos\phi \sin\theta\, y + \mu \sin\phi\, z \\ &\quad + \nu \sin\phi \cos\theta\, x + \nu \sin\phi \sin\theta\, y + \nu \cos\phi\, z. \end{aligned} \tag{12}$$

It is obvious that, with a transformation of coordinates, the right hand side of (12) represents the 3D Fourier Transform $\mathcal{F}_3$ of f at wavenumbers u $=\mu cos\phi\, cos\theta + \nu sin\phi\, cos\theta$, $v=\mu cos\phi\, sin\theta + \nu sin\phi\, sin\theta$ and $w=\mu sin\phi + \nu cos\phi$:

$$[\mathcal{F}_3 f](u, v, w) \int_{-\infty}^{\infty} \int_{-\infty}^{\infty} \int_{-\infty}^{\infty} f(x, y, z) e^{-2\pi i(ux+vy+wz)} dxdydz, \tag{13}$$

which proves the corollary. The quantities u, v and w are wavenumbers in directions x, y and z, respectively. $\square$

The interesting consequence of this corollary is that, given the plane projections, calculating their 2D Fourier Transform, and then computing the inverse 3D Fourier Transform of the resulting set of 2D Fourier transforms after a transformation of coordinates, the original image is directly reconstructed. Figure 4 reports a flowchart of the described image reconstruction procedure. The following subsection provides numerical proof.

3.3. Numerical example of the 3D direct reconstruction

Let us consider an input density function modeled as a cube with a uniform density of 0.5, side length of 0.6, and centered at the origin of the coordinate system (Figure 5a). Inside this cube, two smaller spheres are embedded: one with a density of 0.3, a radius of 0.1, and centered at coordinates (0.05, 0.05, -0.2); the other with a density of 0.1, a radius of 0.05, and centered at (-0.1, 0, 0.1). These variations in density are used to verify the accuracy of the reconstruction, ensuring it can effectively distinguish between different density regions. Although the spheres are not visible from the exterior of the solid cube, Figure 5b illustrates their positions by rendering the cube with partial transparency. It is important to note that for this numerical example, the theoretical framework developed for continuous

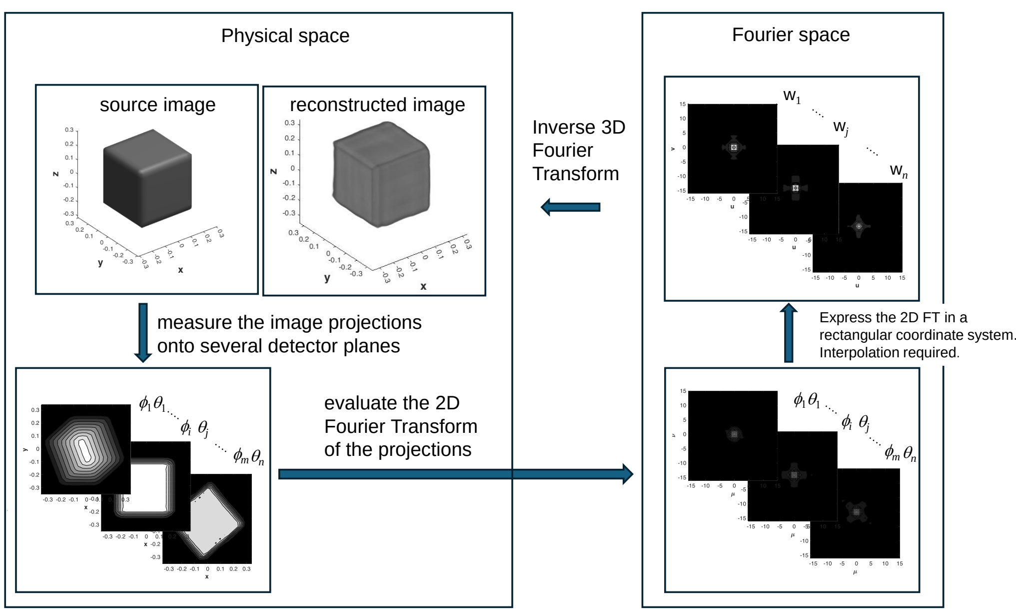

Figure 4: Flowchart of the image reconstruction procedure.

systems in the previous sections has been adapted for use with discrete data. In this case, we employed a total of $N = 64 \times 64 \times 64$ sampling points, with 64 points along each side of the cube. Additionally, $N_{deg} = 12 \times 12 = 144$ spherical projections were taken, with 12 projections for each angle θ and ϕ, respectively. The angular step size was kept constant over π, set to $\pi/12$.

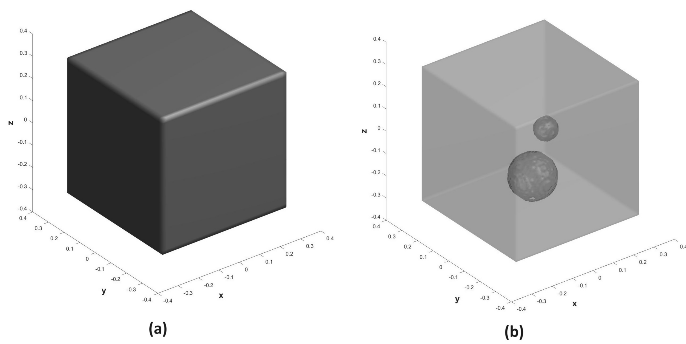

Figure 5: a) 3D density function b) density function made partially transparent to show the embedded spheres

Figures 6a and b provide samples of the spherical projections used for reconstruction, taken at angles $(\theta, \phi) = (\pi/2, 0)$ and $(2\pi/3, 0)$, respectively. Note that the color scale extends beyond 0.5 because it represents line integrals of the density function over the entire domain, rather than local values. Regions of lower density show in fact lower integral values. At this point, it is nexessary that 144 2D Fourier Transforms of the spherical projections are computed. These Transforms are defined on the plane (μ, ν) (Equation (11)). However, computing the inverse 3D Fourier Transform requires knowledge of the data on a Cartesian grid of wavenumbers (u, v, w) (Equation (12)). Therefore, after the transformation of coordinates, discrete data available has to be interpolated to obtain the values onto a regularly spaced Cartesian grid, then 3D inverted. In this way, the reconstructed density function shown in Figure 7a is obtained, matching the original function from Figure 5a. Figures 7b, c, and d present cross-sections of the reconstructed density function along two vertical planes (b,c) and a horizontal plane (d) passing through the origin, with the corresponding color scale. This Figure shows that the embedded spheres are exacly reconstructed not only in terms of position, but also in terms of density. See in fact that the large sphere has high density, while the small one low.

The previous example was implemented using a large number of projections. While reducing the number of projections results in a slightly blurred reconstructed image, even a very limited number of projections still provides a sufficiently clear reconstruction. This effect is illustrated in Figure 8, which shows the reconstructed density function with varying numbers of projections. The source density function is depicted in Figure 8 (a). It is shaped as a cube with a unit density, a side length of 0.2, and is centered at the origin of the coordinate system. A sphere with unit density, a diameter larger than the cube's side, and centered at the origin, was subtracted from the density function, causing its volume to intersect with the cube's faces. Although the image quality decreases as the number of projections is reduced, the shape remains distinctly recognizable even with a very limited number of projections, as few as 9 (Figure 8d).

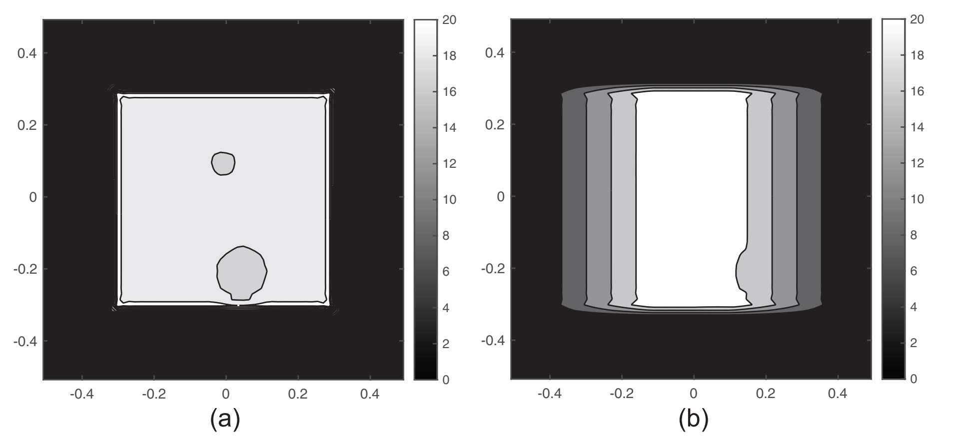

Figure 6: A couple of spherical projections pertaining to angles a) $\theta = \pi/2$, $\phi = 0$ and b) $\theta = 2\pi/3$, $\phi = 0$

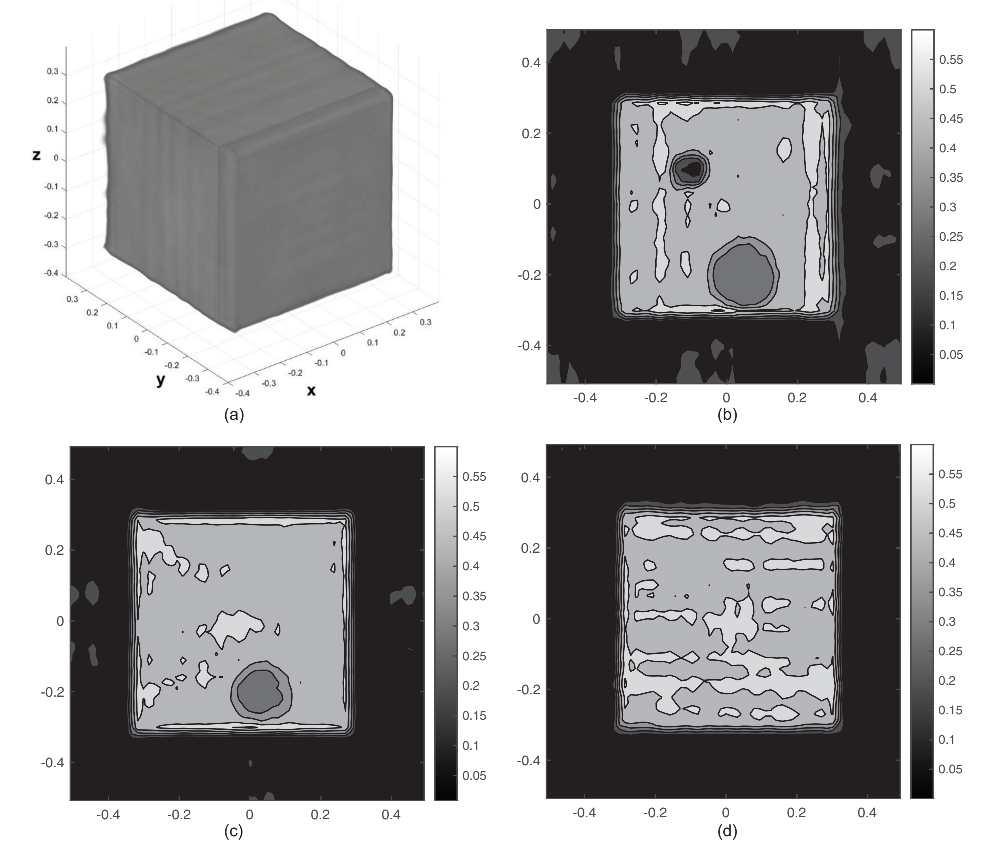

Figure 7: a) Reconstructed image, b) vertical cross section on the xz plane, c) vertical cross section on the yz plane, d) horizontal cross section on the xy plane.

4. 3D Reconstruction of light emission density in PROTO-SPHERA experiment

4.1. The PROTO-SPHERA experiment

PROTO-SPHERA (Spherical Plasma for HElicity Relaxation Assessment) is an innovative magnetic confinement plasma experiment aimed at advancing controlled thermonuclear fusion research. Its goal is to form plasma within a confined environment. Unlike tokamaks, where the plasma forms around a metal centerpost, in PROTO-SPHERA, the plasma forms around a plasma centerpost [3, 27, 31]. Tokamaks, the most extensively studied magnetic fusion configurations, have a non-simply connected geometry, where a central

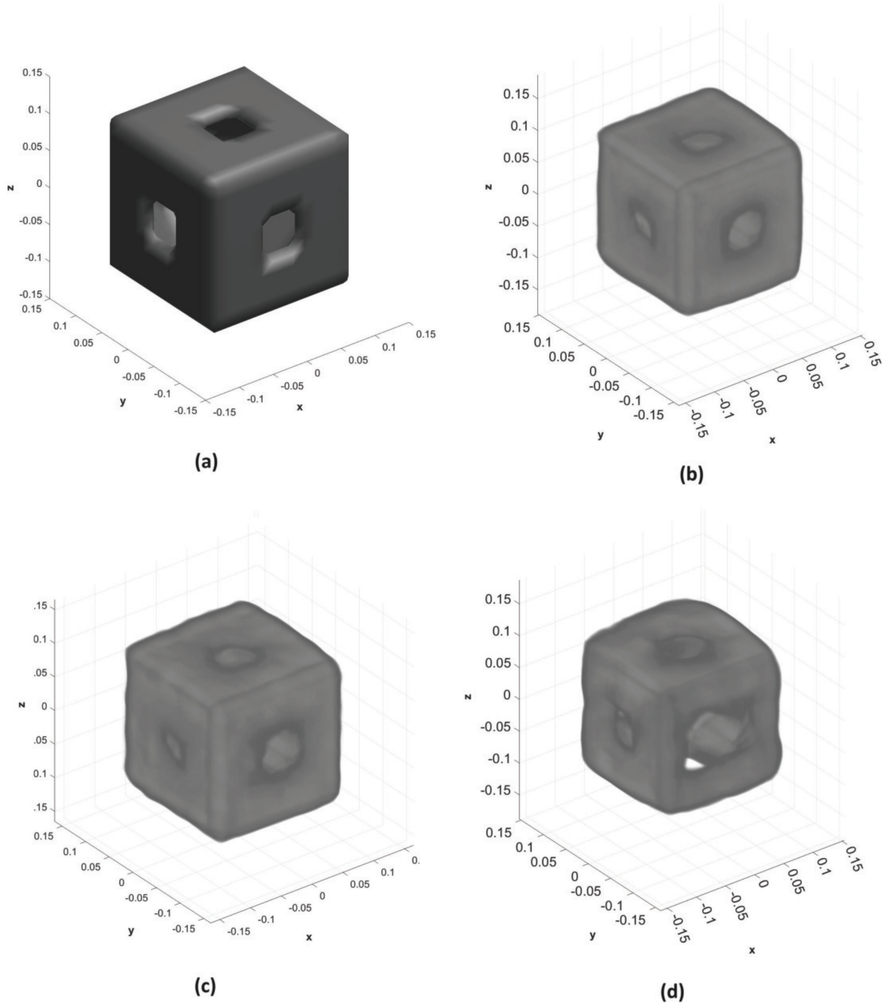

Figure 8: a) Source image and Reconstructed image with b) 12×, c) 6 × 6 and d) 3 × 3 projections.

post—containing the inner part of the toroidal magnet and the ohmic transformer—connects the plasma torus. The development of simply connected magnetic configurations relevant for fusion would significantly simplify the design of fusion reactors. Additionally, the PROTO-SPHERA experiment seeks to emulate astrophysical plasmas, such as jet and torus structures, in a laboratory setting [2].

Figure 9 shows a schematic of the PROTO-SPHERA experiment, which consists of a transparent cylindrical vacuum chamber measuring 2.5 meters in height and 2.0 meters in diameter, held by a metal structure (Figure 9a). The vaccum chamber, surrounded by four columns, is equipped with electrodes at its ends and internal poloidal field coils (Figure 9b). The operating sequence proceeds as follows: the tungsten filaments of the cathode are heated to 2600-2900°C over 30 seconds, while the current in the poloidal field coils is ramped up to its final value. Gas is then introduced through a hollow section in the anode, reaching a pressure of 10^{-2} to 10^{-1} mbar, and a total voltage of 100-350 V is applied between the electrodes, yielding a centerpost current up to 10 kAmp. Under these conditions, cold plasma with an energy in the range of 20-30 eV forms, with an emission concentrated in the visible and ultraviolet spectrum.

To study the plasma formation process and the magneto-hydrodynamic phenomena occurring in the experiment, six high-speed cameras are positioned on the equatorial plane of the chamber, spaced 60 degrees apart (Figure 10). It should be noted that in an ideal scenario free from errors, two cameras placed exactly 180 degrees apart would provide redundant information. However, real-world measurements are inevitably affected by several sources of error. These include, but are not limited to, slight misalignments in camera positioning, optical distortions, slight differences in vignetting due to material objects present inside the vessel, thermal expansion, structural vibrations, and electronic noise. In this context, having views from opposite sides of the plasma increases the robustness of the reconstruction and helps mitigate the effects of such errors. Each camera has a resolution of 640x480 pixels and can capture 600 frames per second. Sample images recorded by the cameras at a specific time instant are shown in Figures 11a and 12a for shots with Helium and Hydrogen, respectively.

Combining the data from the cameras with measurements from a Langmuir probe has provided valuable insights into the dynamics of the plasma torus formation, including its size and emission spectrum. Numerous discharges were produced and observed throughout the experimental campaign.

The images captured by the six cameras are assumed to be parallel projections onto vertical planes corresponding to the camera views of the visible-light emission density, which plays the role of the density function f (Figures 11a and 12a). For each time instant, exploiting the corollary of the Fourier Slice Theorem of Section 3, these source images are 2D-Fourier transformed, then 3D-Fourier inverted to obtain the density of the visible light emitted by the plasma. The only change with respect to the procedure described in Section 3.2 is that, given the positioning of the cameras, the inversion has to be based on a cylindrical set of parallel projections instead of a spherical set, with ϕ fixed. Figures 11b and 12b show the reconstructed plasma light emission distribution derived from the images on the left for Helium and Hydrogen, respectively. It is important to note that the original images contain three layers of information, corresponding to the RGB color channels. The reconstructed images in Figures 11b and 12b are false-color representations, created by combining the RGB channels linearly with the following weighting: 100% Red, 86% Green, and 25% Blue [2].

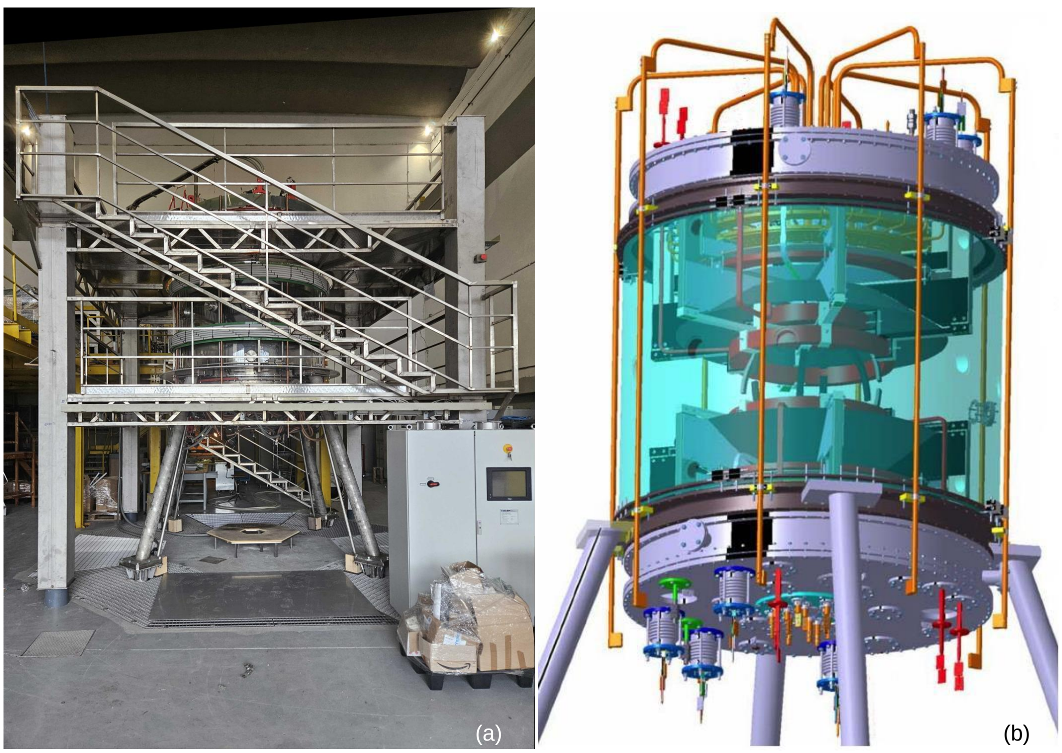

Figure 9: a) Picture of PROTO-SPHERA setup and b) schematic of the machine

4.2. Results and discussion

The proposed 3D tomography technique enabled detailed observation of the plasma torus formation process. The sequence begins with the formation of a plasma column (pinch or centerpost) at a current lower than 10 kAmps.

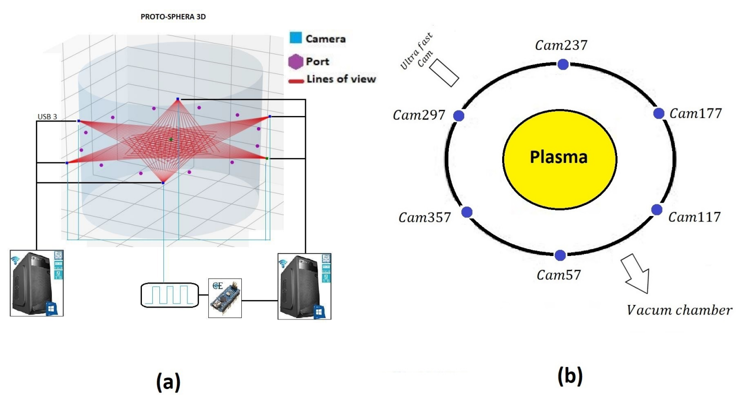

Figure 10: a) Position of the cameras in axonometry b) and plan

As the current reaches this value, the magnetic field lines bend, causing the pinch to become unstable, which leads to the formation of a torus around the centerpost. This progression is visualized in Figure 13 a-h, showing the reconstructed light emission density at eight sequential time steps (each 1/600 s apart) during a Helium plasma discharge. These finding align closely with predictions from magnetohydrodynamic (MHD) models, in particular those presented in the work by García-Martínez et al. [16], whose magnetic field lines at different Lundquist numbers present a striking topological similarity with our emission density reconstruction (see Figure of 8 [16]). The entire torus formation occurs within approximately 8 ms, five time steps intercurring from the arrangements of Figure 13 b to g. The presence of both jets and the torus strongly parallels astrophysical phenomena, as discussed in [2].

Once the spatial distribution of light emission density is known for each time instant, cross-sections can be derived, revealing further insights into plasma dynamics. Figure 14 shows an image of the Helium plasma captured by one of the six cameras (a) and a vertical cross-section (b) of the reconstructed light emission density in true color, taken at the same moment. To create this image, each of the three RGB channels was processed independently to generate a corresponding density function for each color. This cross-sectional view reveals the green color, which was obscured in the camera pictures by the intense orange glow of the 'ionization peel'—the layer between the plasma and the surrounding gas cushion. The correcness of the reconstruction is proved by the appearance of the Langmiur probe and of the copper bars on the right hand side of the picture. These are external conducting copper bars (3 cm in diameter) that connect the two electrodes.

Figure 15 presents vertical cross-sections of the plasma light emission density at the same time instants as Figure 13. These images further confirm the sequence of events leading to the formation of the torus, as described in the previous paragraph. Specifically, Figure 15 illustrates the emergence of a stable pinch (a-b), its progression towards instability (c-f), and ultimately the arrangement of the torus around the centerpost (d-h). Similar patterns, with comparable duration, were observed in other plasma discharges [2, 36]. Figure 16 presents a horizontal cross-section at the equatorial level, enabling observation of the same phenomena from a different perspective. In Figures 16d and 16e, the pinch's instability is particularly evident, as shown by the loss of axial symmetry and the presence of green regions on the right side of the images. The phenomena described, featuring a centerpost around which a toroidal structure forms, show similar morphology with some theoretical results presented in [16], concerning MHD models, in particular, with those displaying the ratio between current density and magnetic field of an equatorial section. Further experimental confirmation of our finding comes from the PROTO-SPHERA research group, who obtained similar results using different reconstruction techniques. Specifically, Figure 17 reproduces a Figure of the work [9], and displays the plasma luminosity obtained through tomographic inversion using Zernike polynomials. The data in this figure refers to earlier experiments conducted with Argon gas and are shown in false colors. Data support the presence of the toroidal light emission structure and of the centerpost observed in our study. In the experiments reported in [9] not all the details of the setup had been finalized.

Additionally, the horizontal cross-section analysis provides insights into plasma stability and torus thickness. Figure 18 illustrates selected horizontal cross-sections of Helium plasma at the equatorial level across sequential times, clearly depicting the torus encircling the centerpost. Notably, the light emission intensity varies over time, suggesting potential correlations with plasma density and stability. These images also allowed for the measurement of torus thickness, defined as the difference between the outer and inner circumferences' radii, which was observed to be between 0.25 and 0.35 m. Note that, in Figure 18, the angle brilliance visible at the four corners is likey due to the reflection of light from the four metal columns supporting the vessel. Similar behaviors were noted for Hydrogen plasma discharges, with an equatorial horizontal cross-section provided in Figure 19 for reference.

5. Conclusions

An imaging technique based on a corollary of the Fourier slice theorem was applied to reconstruct the light emission distribution of magnetically confined plasma in three dimensions. The derived algorithm was used on pictures capturing the visible light emission from Helium and Hydrogen plasmas, recorded by six cameras as part of the PROTO-SPHERA experiment at the ENEA Frascati laboratories. The results demonstrate that six images taken by cameras arranged in cylindrical symmetry enable an accurate 3D reconstruction of the plasma's spatial distribution at different time instants during the experiment. We observed that the plasma torus forms in approximately 8 ms, evolving from a kinked filament caused by the destabilization of the plasma centerpost. This 3D reconstruction allows for cross-sectional analysis, revealing previously hidden green light emission from the core, which had been obscured by the outer orange ionized layer. Additionally, equatorial cross-sections enabled the measurement of the torus thickness, which was found to range between 0.25 and 0.35 meters.

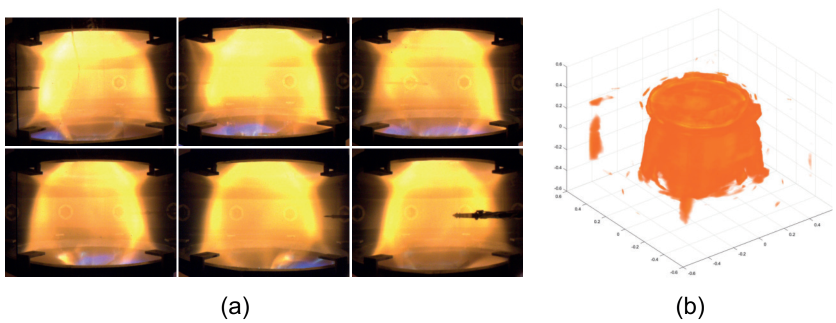

Figure 11: a) Pictures recorded by the six cameras at a given time instant (267 msec) of the PROTO-SPHERA experiment from shot 2505 of Helium b) 3D reconstruction of plasma light emission density

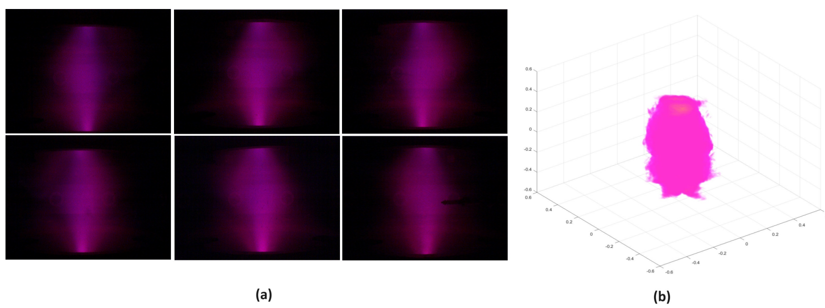

Figure 12: a) Pictures recorded by the six cameras at a given time instant (233msec) of the PROTO-SPHERA experiment from shot 2154 of Hydrogen b) 3D reconstruction of plasma light emission density

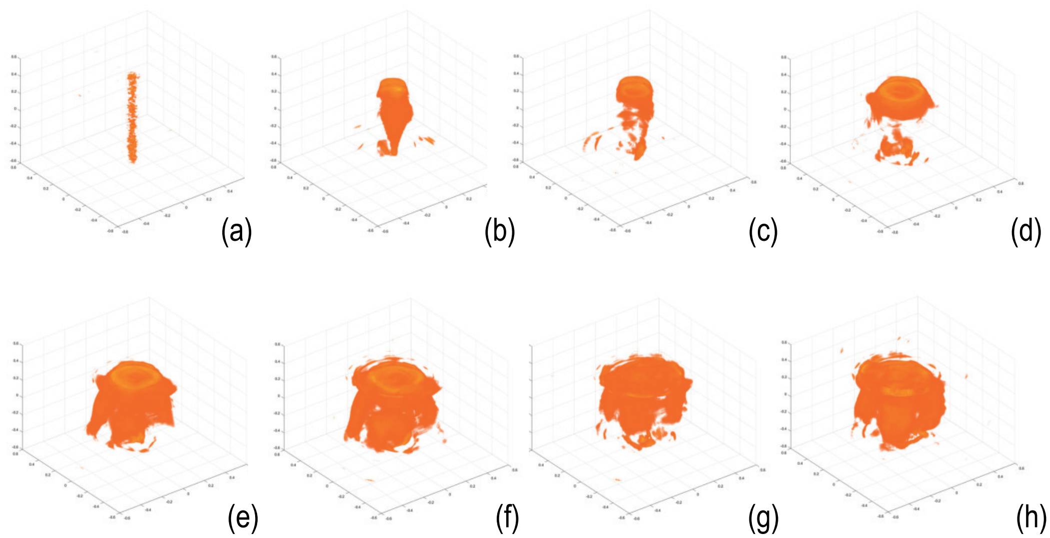

Figure 13: Reconstructed light emission density of Helium discharge 2505 at eight sequential time steps: stable pinch (a-b), pinch instability (c-f), formation of the plasma torus around the pintch (g-h)

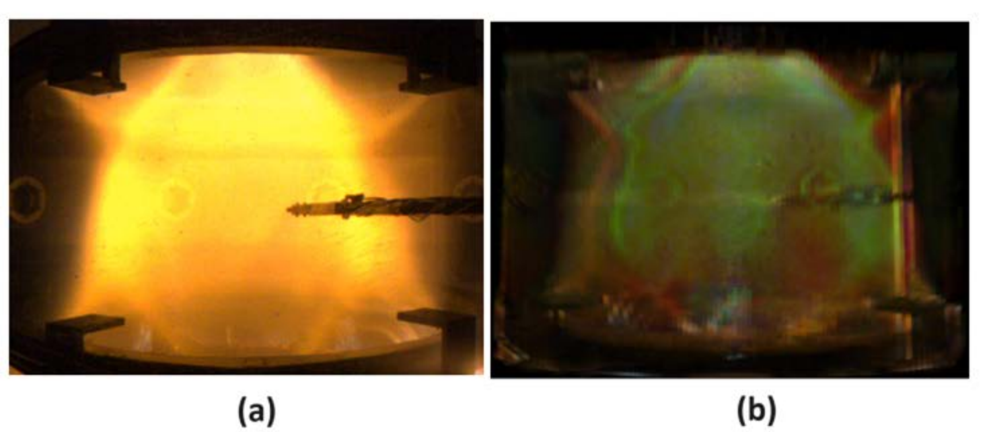

Figure 14: A projection of Helium plasma visible light emission captured by a camera during shot 2141 (a) and cross-section of the reconstructed light emission density in true colors (b).

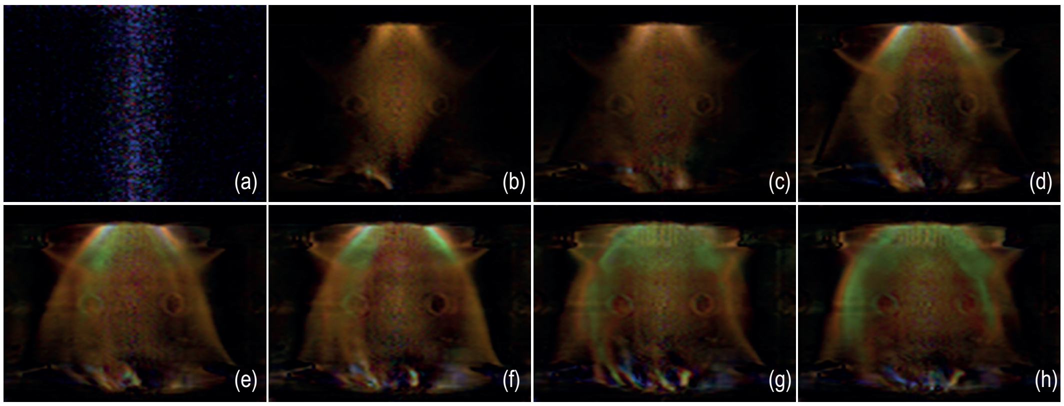

Figure 15: Vertical cross-sections of the reconstructed light emission density of Helium discharge 2505 at the same eight sequential time instants as Figure 12: stable pinch (a-b), pinch instability (c-f), formation of the plasma torus around the pinch (g-h)

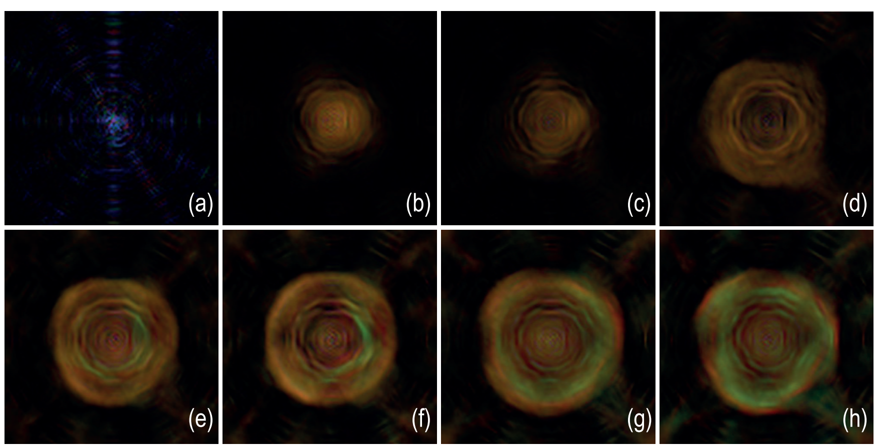

Figure 16: Horizontal cross-sections of the reconstructed light emission density of Helium discharge 2505 at the same eight sequential time instants as Figure 12: stable pinch (a-b), pinch instability (c-f), formation of the plasma torus around the pinch (g-h)

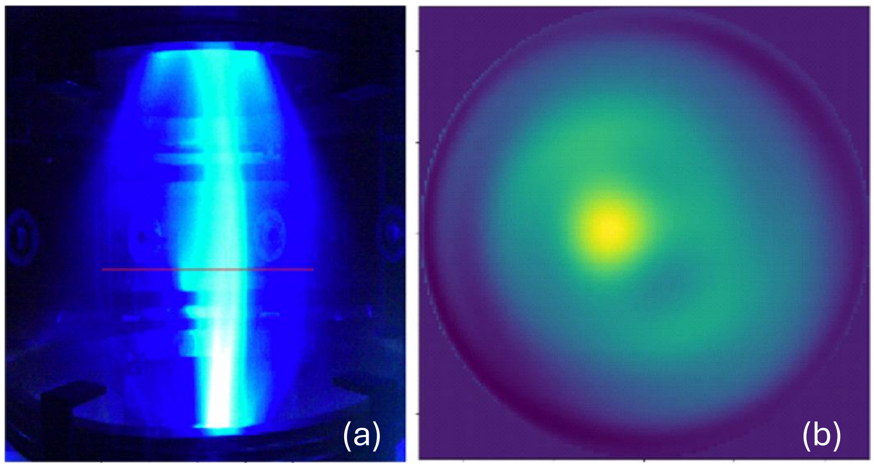

Figure 17: Picture and related equatorial distribution of Argon plasma luminosity obtained by Zernike polynomials inversion [9]

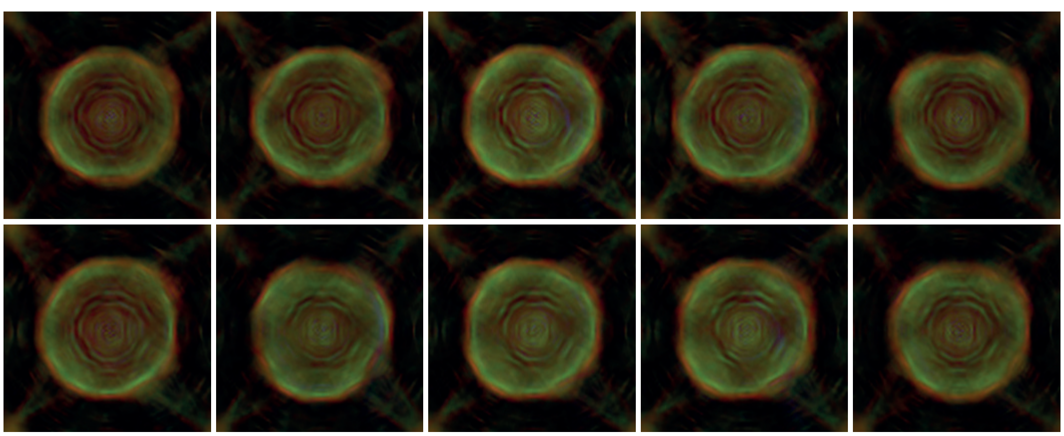

Figure 18: Sequence of reconstructed equatorial cross-sections of light emission density of Helium discharge 2505 at 10 time instants

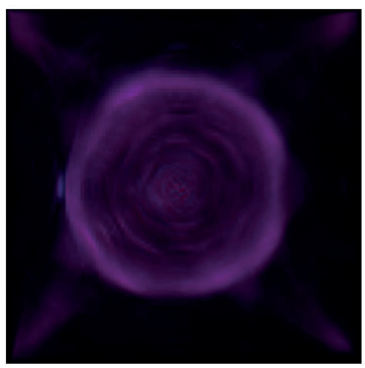

Figure 19: Equatorial cross-section of light emission density of Hydrogen discharge 2154

References

[1] Amir M. Alani, Francesco Soldovieri, Ilaria Catapano, Iraklis Giannakis, Gianluca Gennarelli, Livia Lantini, Giovanni Ludeno, and Fabio Tosti. The use of ground penetrating radar and microwave tomography for the detection of decay and cavities in tree trunks. *Remote Sensing*, 11(18), 2019.

[2] F. Alladio, P. Micozzi, L. Boncagni, A. Pau, S. Naghinajad, S. Macera, Y. Damizia, P. Buratti, F. Filippi, G. Galatola Teka, F. Giammanco, E. Giovannozzi, M. Iafrati, A. Lampasi, and P. Marsili. PROTO-SPHERA: a magnetic confinement experiment which emulates the jet + torus astrophysical plasmas. *Plasma Physics and Controlled Fusion*, 66(3), 2024.

[3] Franco Alladio, Paolo Costa, Alessandro Mancuso, Paolo Micozzi, Stamos Papastergiou, and Francois Rogier. Design of the PROTO-SPHERA experiment and of its first step (MULTI-PINCH). *Nuclear Fusion*, 46:S613–S624, 2006.

[4] Habib Ammari. Tomographic imaging with non-diffracting sources. an introduction. *Mathematics of Emerging Biomedical Imaging*, 28(10):95–106, 2008.

[5] Amir Averbuch and Yoel Shkolnisky. 3D Fourier based discrete Radon transform. *Applied and Computational Harmonic Analysis*, 15(1):33 – 69, 2003.

[6] T. Buzug. *Computed Tomography*. Springer: Berlin, Heidelberg, 2008.

[7] V. Cnudde and M.N. Boone. High-resolution X-ray computed tomography in geosciences: A review of the current technology and applications. *Earth-Science Reviews*, 123:1 – 17, 2013.

[8] A. M. Cormack. Early two-dimensional reconstruction and recent topics stemming from it. *Science*, 209:1482–1486, 1980.

[9] Yacopo Damizia, Matteo Iafrati, Davide Liuzza, Luca Boncagni, Paolo Micozzi, and Franco Alladio. Optical tomography of the plasma on the PROTO-SPHERA experiment. *Fusion Engineering and Design*, 169, 2021.

[10] L. De Chiffre, S. Carmignato, J.-P. Kruth, R. Schmitt, and A. Weckenmann. Industrial applications of computed tomography. *CIRP Annals - Manufacturing Technology*, 63(2):655 – 677, 2014.

[11] S.R. Deans. *The Radon Transform and some of its applications*. Wiley: New York, 1983.

[12] Musa Sani Musa Niyazi Şentürk Fatih Veysel Nurçin Dilber Uzun Ozsahin, Berna Uzun and Ilker Ozsahin. Evaluating nuclear medicine imaging devices using fuzzy PROMETHEE method. *Procedia computer science*, 120:699–705, 2017.

[13] S. Donato, L. Brombal, L.M. Arana Peña, F. Arfelli, A. Contillo, P. Delogu, F. Di Lillo, V. Di Trapani, V. Fanti, R. Longo, P. Oliva, L. Rigon, L. Stori, G. Tromba, and B. Golosio. Optimization of a customized simultaneous algebraic reconstruction technique algorithm for phase-contrast breast computed tomography. *Physics in Medicine and Biology*, 67(9), 2022.

[14] Mario D'Acunto, Antonio Benassi, Davide Moroni, and Ovidio Salvetti. 3D image reconstruction using Radon transform. *Signal, Image and Video Processing*, 10(1):1 – 8, 2016.

[15] Jeffrey Fessler. Optimization methods for magnetic resonance image reconstruction: Key models and optimization algorithms. *IEEE signal processing magazine*, 37(1):33–40, 2020.

[16] Pablo Luis García-Martínez, Leandro Gabriel Lampugnani, and Ricardo Farengo. Effect of the helicity injection rate and the Lundquist number on spheromak sustainment. *Physics of Plasmas*, 21(12), 2014.

[17] Richard Gordon, Robert Bender, and Gabor T. Herman. Algebraic reconstruction techniques (ART) for three-dimensional electron microscopy and X-ray photography. *Journal of Theoretical Biology*, 29(3):471–476,IN1–IN2,477–481, 1970.

[18] David Gottlieb, Bertil Gustaffson, and Patrick Forssen. On the direct Fourier method for computed tomography. *IEEE Transactions on Medical Imaging*, 19(3):223–232, 2000.

[19] R.S. Granetz and P. Smeulders. X-ray tomography on JET. *Nuclear Fusion*, 28(3):457 – 476, 1988.

[20] B Gustaffson. Mathematics for computed tomography. *Physica Scripta*, T61:38– 43, 1996.

[21] G. N. Hounsfield. Computerized transverse axial scanning (tomography): Part I. description of system. *British Journal of Radiology*, 46(3):1016–1022, 1973.

[22] P. Huthwaite. Guided wave tomography with an improved scattering model. *Proceedings of the Royal Society A: Mathematical, Physical and Eng. Sciences*, 472(2195), 2016.

[23] A. Jardin, J. Bielecki, D. Mazon, Y. Peysson, K. Król, D. Dworak, and M. Scholz. Implementing an X-ray tomography method for fusion devices. *European Physical Journal Plus*, 136(7), 2021.

[24] A. C. Kak and M. Slaney. *Principles of Computerized Tomographic Imaging*. IEEE press, 1988.

[25] Avinash C. Kak. Computerized tomography with X-ray, emission, and ultrasound sources. *Proceedings of the IEEE*, 67(9):1245 – 1272, 1979.

[26] Mohd Taufiq Mohd Khairi, Sallehuddin Ibrahim, Mohd Amri Md Yunus, M. Faramarzi, Goh Pei Sean, Jaysuman Pusppanathan, and A. Abid. Ultrasound computed tomography for material inspection: Principles, design and applications. *Measurement: Journal of the International Measurement Confederation*, 146:490 – 523, 2019.

[27] Alessandro Lampasi, Giuseppe Maffia, Franco Alladio, Luca Boncagni, Federica Causa, Edmondo Giovannozzi, Luigi Andrea Grosso, Alessandro Mancuso, Paolo Micozzi, Valerio Piergotti, Giuliano Rocchi, Alessandro Sibio, Benedetto Tilia, and Vincenzo Zanza. Progress of the plasma centerpost for the PROTO-SPHERA spherical tokamak. *Energies*, 9(7), 2016.

[28] Xin Li, Yudong Lu, Xiaozhou Zhang, Wen Fan, Yangchun Lu, and Wangsheng Pan. Quantification of macropores of malan loess and the hydraulic significance on slope stability by x-ray computed tomography. *Environmental Earth Sciences*, 78(16), 2019.

[29] E. Maire and P.J. Withers. Quantitative X-ray tomography. *Int. Materials Reviews*, 59(1):1 – 43, 2014.

[30] Francisco A. Matos, Diogo R. Ferreira, and Pedro J. Carvalho. Deep learning for plasma tomography using the bolometer system at JET. *Fusion Engineering and Design*, 114:18 – 25, 2017.

[31] Paolo Micozzi, Franco Alladio, Alessandro Mancuso, Vincenzo Zanza, Gerarda Apruzzese, Francesca Bpmbarda, Luca Boncagni, Paolo Buratti, Francesco Filippi, Giuselle Galatola Teka, Francesco Giammarco, Edmondo Giovannozzi, Andrea Grosso, Matteo Iafrati, Alessandro Lampasi, Violeta Lazic, Simone Magagnino, Simone Mannori, Paolo Marsili, Paolo Piergotti, Giuliano Rocchi, Alessandro Sibio, Benedetto Tilia, and Onofrio Tudisco. Final results of the first phase of the PROTO-SPHERA experiment: obtainment of the full current stable screw pinch and first evidences of the jet + torus combined plasma configurationy. *Plasma Science and Technology*, 26:025103, 2024.

[32] Jan Mlynar, Teddy Craciunescu, Diogo R. Ferreira, Pedro Carvalho, Ondrej Ficker, Ondrej Grover, Martin Imrisek, and Jakub Svoboda. Current Research into Applications of Tomography for Fusion Diagnostics. *Journal of Fusion Energy*, 38(3-4):458 – 466, 2019.

[33] M. Odstrcil, J. Mlynar, T. Odstrcil, B. Alper, and A. Murari. Modern numerical methods for plasma tomography optimisation. *Nuclear Instruments and Methods in Physics Research, Section A: Accelerators, Spectrometers, Detectors and Associated Equipment*, 686:156 – 161, 2012.

[34] Tugba Ozge Onur. An application of filtered back projection method for computed tomography images. *International Review of Applied Sciences and Engineering*, 12(2):194 – 200, 2021.

[35] Yongwoo Park, Un-Chul Paek, and Dug Young Kim. Characterization of a stress-applied polarization-maintaining (PM) fiberthrough photoelastic tomography. *Journal of lightwave technology*, 21(4):997 – 1004, 2003.

[36] A. Pau, S. Naghinajad, F. Alladio, P. Micozzi, and L. Boncagni. 3D tomography of Hydrogen and Helium plasma produced in th PROTO-SPHERA experiment. In *Proceedings of the ASME 2024 51st Annual*

Review Progress in Quantitative Nondestructive Evaluation QNDE2024, pages 1–7, Denver, Colorado, July 2024.

[37] Johann Radon. On the determination of functions from their integral values along certain manifolds (translation from the original German text published in Berichte der Sächsischen Akademie der Wissenschaft, vol. 69, pp. 262-277, 1917). *IEEE Transactions on Medical Imaging*, MI-5(4):170–176, 1986.

[38] L. Schoeman, P. Williams, A. du Plessis, and M. Manley. X-ray micro-computed tomography (μCT) for non-destructive characterisation of food microstructure. *Trends in Food Science and Technology*, 47:10 – 24, 2016.

[39] James Anthony Seibert. Iterative reconstruction: how it works, how to apply it. *Pediatric Radiology*, 44(3):431 – 439, 2014.

[40] Wolfram Stiller. Basics of iterative reconstruction methods in computed tomography: A vendor-independent overview. *European Journal of Radiology*, 109:147 – 154, 2018.

[41] M.L.L. Wijerathne, Kenji Oguni, and Muneo Hori. Tensor field tomography based on 3D photoelasticity. *Mechanics of Materials*, 34(9):533 – 545, 2002.

[42] Tao Zhang, Yuxiang Xing, Li Zhang, Xin Jin, Hewei Gao, and Zhiqiang Chen. Stationary computed tomography with source and detector in linear symmetric geometry: Direct filtered backprojection reconstruction. *Medical physics*, 47(5):2222–2236, 2020.

[43] Yingying Zhang-O'Connor and Jeffrey A. Fessler. Fourier-based forward and back-projectors in iterative fan-beam tomographic image reconstruction. *IEEE Transactions on Medical Imaging*, 25(5):582 – 589, 2006.

[44] Dominique Zosso, Benoît Le Callennec, Meritxell Bach Cuadra, Kamiar Aminian, Brigitte M. Jolles, and Jean-Philippe Thiran. Bi-planar 2D-to-3D registration in fourier domain for stereoscopic X-ray motion tracking. volume 6914, 2008.

Declaration of interests

☒The authors declare that they have no known competing financial interests or personal relationships that could have appeared to influence the work reported in this paper.

☐The authors declare the following financial interests/personal relationships which may be considered as potential competing interests:

Title Page

Title:

3D tomographic reconstruction of light emission density of plasma in the PROTO-SPHERA experiment

Author Information

Author names:

Annamaria Pau[a]*, corresponding author,* annamaria.pau@uniroma1.it
Shayesteh Naghinajad[a]*,* shayesteh.naghinajad94@gmail.com
Franco Alladio[b]*,* franco.alladio@protosphera.it
Paolo Micozzi[c]*,* paolo.micozzi@enea.it
Luca Boncagni[c]*,* luca.boncagni@enea.it

Affiliations:

[a] *Department of Structural and Geotchnical Engineering, Sapienza University of Rome, via Eudossiana 18, 00184 Roma, Italy,*

[b]*INAF-IAPS National Institute of Astrophysics, Via del Fosso del Cavaliere 100, 00133 Roma, Italy*

[c]*Nuclear Research Department, ENEA Italian National Agency for Technology, Energy and Sustainable Economic Development, Via Enrico Fermi 45, 00044 Frascati (RM), Italy*

Corresponding author:

Annamaria Pau, annamaria.pau@uniroma1.it

Annamaria Pau gratefully acknowledges the funding contribution from National Center on HPC, Big Data and Quantum Computing CN00000013. This manuscript reflects only the authors' views and opinions, neither the European Union nor the European Commission can be considered responsible for them.